

Supplemental Data

Cell, Volume 133

Cell Shape and Negative Links in Regulatory Motifs Together Control Spatial Information Flow in Signaling Networks

Susana R. Neves, Panayiotis Tsokas, Anamika Sarkar, Elizabeth A. Grace, Padmini Rangamani, Stephen M. Taubenfeld, Cristina M. Alberini, James C. Schaff, Robert D. Blitzer, Ion I. Moraru, and Ravi Iyengar

Contents:

Supplemental Text

 Methods

 Mathematical Representation of microdomains

 Description of Simulations

Supplemental Figures S1-S23

Supplemental Tables S1-S7

Supplemental Movies SM1-SM6

Supplemental References

Supplemental Text

Methods:

Simulation:

Modeling was conducted in the Virtual Cell modeling environment (S1). Initially, the model was developed as an ordinary differential equation (ODE) compartmental model, and then converted into a spatial partial differential equation (PDE) model to incorporate the constraints of the geometry and diffusion. Concentrations and reaction rates were obtained from the experimental literature (see tables S1 and S2) as described previously (S2). Localization within the models was specified according to the experimental literature dealing with subcellular location. Experimentally determined flux value for cAMP was used (S3). For other components, such as MAPK, flux values were approximated based on the molecular weight, and were adjusted to account for molecular crowding and tertiary molecular structure (see table S2 for values, see Box S1 for example).

Initial concentrations are displayed in units of molecules/ μm^2 for membrane components, and μM for cytosolic components (see Table S2; for those components not shown, the initial concentration was set at zero). Components were then placed in the appropriate compartment, and their initial concentration was

Box 1: Example of calculation of diffusion coefficients based on molecular weight

Molecular weight of serum albumin = 68.5 KDa
Molecular weight of component = M KDa
Diffusion coefficient of serum albumin = $6.1 \mu\text{m}^2 \cdot \text{s}^{-1}$
Diffusion coefficient of component = $x \mu\text{m}^2 \cdot \text{s}^{-1}$

$$x = \left(\frac{68.5}{M} \right)^{\frac{1}{3}} \quad (6.1)$$

based experimentally determined values (Table S1). Realistic cell geometries were traced from microscopic images in the literature (see table S3) and the compartments were mapped on to the geometry. Compartmental models were run using the LSODA ODE solver. Spatial model simulations were run using the regular grid, finite volume solver. Steady state concentrations were obtained by running the model starting with the initial concentrations without ligand stimulation, until all the components reached steady state. Detailed descriptions relating to simulations of each particular geometry are given in table S3. Complete models, parameters and geometry are available at <http://vcell.org/>.

Experiments:

Primary Hippocampal Cultures:

Hippocampal cultures were prepared as described previously (S4). Briefly, the hippocampi from embryonic day 18 rat fetuses were dissected, digested with trypsin and mechanically triturated. Dissociated neurons were plated on poly-lysine coated coverslips. Four hours post-plating, media was replaced with serum-free media containing B27 supplement (Invitrogen) and cultured for 3-6 days (Days in Vitro, DIV). The protocols for animal experiments have been approved by the Mount Sinai IACUC.

Transfections

Neurons were transfected with Lipofectamine 2000 (Invitrogen). Briefly, $1 \mu\text{g}$ cDNA was complexed to $1 \mu\text{L}$ lipofectamine 2000 in a total volume of $100 \mu\text{L}$ per 35 mm dishes. The DNA/lipid complex was added to the neurons. Neurons were imaged 24 hours post transfection.

FRET imaging

Primary hippocampal neurons transfected with EPAC1 were imaged in a Zeiss LSM meta-510 confocal microscope. The donor fluorophore was excited with the 458 nm laser, and detected with bandpass filter $475\text{-}525 \text{ nm}$. FRET signal was detected with bandpass filter $560\text{-}615 \text{ nm}$. Acceptor fluorophore was excited with 514 nm laser and detected with bandpass filter $560\text{-}615 \text{ nm}$. Images were corrected for photobleaching, bleedthru and scaled. FRET was calculated using the nF method (S5) in Volocity (Improvision).

Hippocampal Slice Preparation:

Hippocampal slice preparation has been previously described in detail (S6). Briefly, male adult Sprague Dawley rats were anesthetized and euthanized, their brains removed and hippocampi dissected. 500 μ m-thick hippocampal slices were obtained. After a 2 hour recovery in a humidified chamber, hippocampal slices were treated with various agents. Treatments for immunohistochemistry experiments were as follow: 10 μ M rolipram (Calbiochem) for 30 min, 10 μ M isoproterenol (Sigma) for 20 min or 10 μ M rolipram for 30 min followed by 10 μ M isoproterenol for 20 min. In some experiments rolipram was replaced with okadaic acid, 1 μ M (Calbiochem). Nifedipine, 10 μ M (Tocris) and Tetrodotoxin, 1 μ M (Calbiochem) were added to all conditions to prevent any calcium or depolarization-dependent signaling. For dose-response curves, isoproterenol was added for 10 min. For time courses, the concentration of isoproterenol used was 10 μ M. Slices were fixed in 4% Paraformaldehyde at 4°C for immunofluorescence or flash-frozen and stored at -80 for immunoblotting or cAMP assay.

Antisense Oligonucleotide Design

Antisense oligonucleotides were designed against the products of the rat gene PTPRR (GeneID 94202). The isoforms targeted by antisense oligonucleotides were MVQP (Pubmed ID= BC089186), MIIY (Pubmed ID =U14914), and MDID (Pubmed ID= D64050). The antisense oligonucleotides sequences are (MVQP 5'-TGGACCATGCTGTGGGC-3') its scrambled control is (5'-CGCCTTGTGATACGGGG-3') ; (MIIY 5'-ACCTATAAATGATCATCAA-3') and its scrambled control is (5'-CCCCAAATAAAAGATTTAAT-3'); (MDID 5'-GCAGTGTCGAGTGTGCG-3') and its scrambled control is (5'-TACTATGGGTCTGCTGGG-3'). The scrambled oligonucleotides, which served as a control, were designed to lack homology to any rat sequence in GenBank. They contained the same base composition but in a randomized order. Both antisense and scrambled oligonucleotides were phosphorothioated on the three terminal bases of both 5' and 3' ends to increase their stability and were reverse phase purified (GeneLink).

Antisense Oligonucleotide Treatment

Implantation of cannulas has been described elsewhere in detail (S7). Briefly, male Sprague Dawley rats were anesthetized with Ketamine-Xylazine (80 mg/kg, 5 mg/kg, i.p.), and stereotaxic procedures were used to implant stainless steel guided cannulae, bilaterally into the hippocampus (4 mm posterior to bregma; 2.6 mm lateral from midline and 2.0 mm ventral). After a 7-day recovery period, rats were injected (2 nmol in 1 μ l) every 12 hours for 48 hours (a total of 4 injections) with either PTPRR antisense combo or scrambled oligodeoxynucleotide both diluted in phosphate-buffered saline (PBS), pH 7.4. Rats were sacrificed 12-16 hours post last injection. This protocol has been approved by the Mount Sinai IUACUC

Antisense Oligonucleotide Validation

Tissue slices from antisense or scrambled treated hippocampi were processed for RNA isolation using Trizol reagent (Invitrogen). 0.5 μ g of total RNA was used per reaction. Real-time PCR was performed with a Roche lightcycler with a Qiagen QuantiTect One Step RTPCR SYBR green kit (Qiagen) according to manufacturer's instructions. Primers were designed using OMIGA design software (accelrys) and chosen for having the same melting temperatures and amplifying a region of 300 bp or less. The primers are: MVQP_up 5'-AAGACCATTTTGCCAAATCC-3'; MVQP_dw 5'-CGATGACCAGAACCTCAACC-3'; MIIY_up 5'-TCCTAGACCTGCATATGACC-3'; MIIY_dw 5'-ACTCTGACGCAAACATCC-3'; MDID_up 5'-CTGCAAAATGGATATAGACAAGC-3'; MDID_dw 5'-CAAACCTGTGGTAAACTCTGACG-3'. Real time RTPCR conditions were as follows: Reverse transcription, 50°C for 20 min, PCR activation step 95°C for 15 min and 40 cycles of 94°C denaturing temperature (15 s), 55°C annealing temperature (25 s), and 72°C elongation temperature (10 s). Melting curve analysis was performed to check for a single amplicon and was further verified by size using gel electrophoresis. Lightcycler software was used to determine crossing points using the second derivative method. Data were further analyzed by the $2^{-\Delta\Delta C_T}$ method as described by Livak and Schmittgen (S8) and are presented as fold increase normalized to housekeeping gene mRNA (ribosomal protein rPL7).

Immunohistochemistry:

Immunohistochemistry procedure is detailed elsewhere (S6). After washing, slices were subsectioned to 40 μ m on a vibratome (Leica VT 1000S vibratome). Sections were blocked with 10% normal goat serum (vector), 1% BSA, and 0.01% Na-azide in PBS. The sections were incubated overnight at 4°C, in 1% BSA with the appropriate antibodies: rabbit-polyclonal P-MAPK (cell signaling), mouse- monoclonal Tubulin

(Sigma), rabbit-polyclonal PP2A (cell signaling), rabbit-polyclonal PDE4 (Abcam), rabbit polyclonal P-MEK (cell signaling). After washes, sections were incubated with secondary antibodies complexed to either Alexa Fluor 568 or Alexa Fluor 488 dyes (Invitrogen). After washing, the sections were mounted using vectashield (Vector) and imaged using a Zeiss LSM meta-510 confocal microscope. Contrast and brightness were constant for all sections from the same experiment. Images' mean intensities were obtained by tracing the cell body region and stratum pyramidale using Kodak 1D software (Kodak Scientific Imaging System). Statistical significance was determined using two-tailed *t* tests.

Preparation of protein extracts and immunoblotting

Two slices per condition were homogenized in ice-cold lysis buffer using a motorized Potter-Elvehjem homogenizer. The lysis buffer consisted of 50 mM Tris-HCl, pH 7.4, 150 mM NaCl, 1 mM EDTA, 0.25% Sodium Deoxycholate, 1% NP-40, 1 mM PMSF, 1 µg/ml Aprotinin, 1 µg/ml Leupeptin, 1 µg/ml Pepstatin, 1 mM Sodium orthovanadate, 1 mM Sodium Fluoride, and 10 mM beta-glycerolphosphate. Lysates were cleared by centrifugation 12,000 g for 10 min. Protein concentration was determined using Bradford reagent (Biorad)(S9). 20 µg of protein were loaded per well, into 10% SDS-PAGE and transferred to supported nitrocellulose membranes (pore size 0.2 µm, Biorad), followed by immunoblotting and chemiluminescence detection. The following antibodies were used: P-MAPK, rabbit-polyclonal (Cell Signaling), MAPK, rabbit-polyclonal (Cell signaling), tubulin mouse-monoclonal (Sigma). Films were scanned, and the net intensity was recorded. Values are normalized to basal.

Measurement of intracellular cAMP

Intracellular cAMP was measured using an immunoenzymatic commercial kit (Amersham-Biosciences, RPN 225), following the manufacturer's protocol. Two slices per condition were homogenized in manufacturers' buffer 1B. cAMP results are presented as fold change over basal. Statistical significance was determined using two-tailed *t*-tests. EC50 values were calculated using PRISM (Graphpad Software).

Curve Fitting Analysis

Curve fitting analysis was done in Matlab (Mathwork) and is explained in detail in the section "Curve fitting analysis" of the next section, that details the "Mathematical representation of microdomain"

Mathematical representation of microdomains

A simple mathematical representation of the dynamics of a microdomain would include the slope of the concentration gradient, the boundary of the domain as a function of cell shape, and all the biochemical reactions. All of these parameters vary as a function of both time and space. All of these parameters vary as a function of both time and space. To obtain such description, we developed a mathematical representation from numerical simulations. We approximated the realistic geometry of a neuron into simpler, mathematically well-defined shapes. This conversion is described in detail in the following section and Fig S4. Using simulations (Fig S5A), curve fitting (Fig S6) and a set of simple algebraic operations we obtained a relationship between microdomain dynamics, shape and reaction rates. The derivation of this relationship is described in detail in the Supplementary Materials and equation is shown as equation S16 and in Fig S7B. We then used the equation (Fig S7B) to estimate the length of the PKA microdomain and compare the concentration of cAMP at the microdomain boundary from the simulations to what was observed experimentally in Bacskai et al., (1993). For this comparison we first determined the length of PKA microdomain (Fig S7C) and the corresponding cAMP levels from the numerical simulation is shown in Fig S7D. We then compared the mathematically- obtained value for the length of PKA and its corresponding simulated cAMP concentrations to the experimentally observed values which Tsien and coworkers had estimated from an *in vitro* FRET experiment (Fig S7E taken from (S10)). At the calculated length of 48 μm , the simulated cAMP value is 0.35 μM , compared to experimental value of $\sim 0.33 \mu\text{M}$, indicating qualitative agreement between simulations and experiments (Fig S7F). This fitting exercise validates our model. The equation S16 is an initial attempt to describe the relationship between characteristics of the microdomain and the physical and chemical determinants of the system. Equation S16 is obtained from curve fitting and cannot be used analytically.

Curve Fitting

We used the simulation results of the model of the neuronal geometry (S11) shown in fig S5. The gradient of cAMP over the entire neuronal geometry, after 600 s of stimulus, is shown in Fig. S5A. A gradient of cAMP from tip of dendrite to cell body was always observed. Such a gradient is likely to arise from the interactions chemical and physical parameters of the system. To define the interactive relationships between the biochemical and physical factors that contribute to the dynamics of such a gradient, we have simplified the geometry of a neuron by representing the cell body as an ellipse and one dendrite as a triangle. The red dash line (Fig. S4A) shows the contour of the simplified geometry, and the gradient of cAMP, after 600 s, (Fig. S4B). A diagram depicting the simplified geometry of a neuron with all the geometrical parameters used for the mathematical analysis is shown in detail in Fig. S4C. We then developed the relationship between these geometrical parameters and concentration gradient of the signaling components within the microdomain.

I. Quantitative relationship between the microdomain characteristics (length) and of the geometry of the sub-cellular structures and activity of the signaling components

To characterize the boundary of the microdomain as a function of the change in the rate of the stimulus-induced production of a component, and the change in the width of the dendrite (w_i), we have normalized both the length scale and the concentration of the signaling component.

Normalization of length scale

We define the normalized length scale (ξ) as

$$\xi_i = \frac{l_i w_i}{l_D w_D} \quad (S1)$$

at each point i on the length scale, l . The terms l_i , w_i , l_D , w_D are defined in the figure legend of the Fig. S13.

Normalization of the concentration of the signaling molecule

Let $C(l_i, t)$ define the concentration of a signaling molecule SM (eg. cAMP) at the position, l_i , at time t . The values of the concentration of the components at each length, l_i , for all time points, are obtained from the numerical simulations. We define a non-dimensional term, *FMC* (Fraction of Maximal Concentration), as,

$$FMC(l_i, t) = \frac{C(l_i, t)}{C_{max}}, \quad (S2)$$

where C_{max} is the maximum value of $C(l_i, t)$ for all lengths and time.

Definition of the length of the microdomain

We define the length of the microdomain, l_{md} , as the length of the dendrite where $FMC(l_i, t) \geq th_{COL_md}$ for all $l_i \leq l_{md}$ at every time t . The threshold th defines

$FMC \geq defined\ COL$. The term COL in th_{COL_md} represents the cut off limit and is a user defined value of the concentration of the component of interest within the microdomain. The biological basis for COL is the concentration value of the modulated upstream signaling component required to elicit change in activity of the immediate downstream component leading to signal propagation.

Curve Fitting Analysis

We have done curve fitting analysis to find the functional dependence of *FMC* on t and ξ_i . For our curve fitting analysis, we chose the geometry described in fig S4 (b). We ran the model as described in Tables S1-S4, in Virtual Cell for 600 s. We then obtained the numerical values of the signaling molecules of interest (SMI i.e. cAMP) along the length of the extended dendrite (or the extended triangle) at different

time points. For this particular example, $l_D = 26.7 \mu\text{m}$ and $w_D = 16.57 \mu\text{m}$. For this analysis we have assumed that the curve fitting function is independent of diffusion.

We used the MATLAB function ‘*expfit*’ (A MATLAB function which performs parameter estimation for exponential data) to find the best fitted function (by trial and error) that represents the relationship between *FMC* and ζ_i optimally. After obtaining the functional form of the fitted curve, we conducted additional algebraic operations on the function (Section II) to obtain a relationship between the rate of change of the length of the microdomain to (a) the rate of change of the concentration of the SMI at each location within the domain, (b) subcellular geometry and (c) biochemical parameters controlling the rate of production and degradation of the SMI.

Relationship between *FMC* and ζ_i

From curve fitting we find the relationship between *FMC* and ζ_i to be

$$FMC(l_i, t) = k_3(t) \exp(-k_2 \zeta_i^{k_1}) \quad (S3)$$

The parameters k_1 , k_2 , and k_3 are non dimensional fitting parameters. In general, these parameters vary with time. For simplification purposes, k_1 and k_2 are assumed to be independent of time within a defined time range. When k_1 and k_2 are assumed to be independent of time, the maximum error between simulated and fitted results is 8%. We have calculated the values of k_1 and k_2 at the time when $C(l_i, t) = C_{max}$ and have used these values to calculate the *FMC* using Eq (S3), for a time series. With this assumption of k_1 and k_2 to be independent of time, Eq (S3) is now represented as a variable separable form of time and space.

Biological definitions of k_1 , k_2 , k_3

Empirically, the parameter k_1 represents the production of the SMI while k_2 represents the degradation of the SMI. Figure S6 shows the plot of change of *FMC* with the normalized length ζ_i , for numerical values (red curve) for cAMP at different times. The numerical values and fitted results show good agreement.

For example, for cAMP, the fitted values of k_1 and k_2 , at 600 s, when cAMP reaches steady state are 0.56 and 2.24, respectively. From the biochemical parameters (described in Table S2)

$$\begin{aligned} k_1 &= \frac{k_{cat} \text{ of Adenylyl Cyclase}}{k_{cat} \text{ of phosphorylated PDE4}} \\ &= \frac{\text{production of cAMP}}{\text{degradation of cAMP}} \\ &= \frac{8.5 \text{ s}^{-1}}{20 \text{ s}^{-1}} \\ &= 0.425 \text{ (observed value 0.56)} \end{aligned}$$

$$\begin{aligned} k_2 &= \frac{k_{cat} \text{ of phosphorylated PDE4}}{k_{cat} \text{ of Adenylyl cyclase}} \\ &= \frac{\text{degradation of cAMP}}{\text{production of cAMP}} \\ &= \frac{20 \text{ s}^{-1}}{8.5 \text{ s}^{-1}} \\ &= 2.35 \text{ (observed value 2.24)} \end{aligned}$$

For cAMP, k_1 and k_2 represent relatively simple terms and they turn out to be the reciprocals of each other. However, when SMI are downstream components, k_1 and k_2 will represent a complex relationship between production and degradation kinetic constants for each of the upstream components required for signal propagation. Such complex relationships may not necessarily result in an inverse relationship between k_1 and k_2 .

The parameter k_3 is defined as:

$$k_3 = \frac{C_{\max_t}(t)}{C_{\max}} \quad (\text{S4})$$

$C_{\max_t}(t) = \max(C(l_i, t_p))$, where t_p is a particular time. It should be noted that k_3 is dimensionless but not time-independent. Note that in Figure S22, k_3 changes from 0.47 at 50 s to 0.85 at 100 s to 0.89 at 600 s, while k_1 and k_2 remain approximately constant.

II. Explicit description of length of microdomain as a function of rate of change of concentration of SMI at particular location and width of the dendrite

From Eq (S3) we see that FMC and ξ_i are exponentially related. By taking natural log on both sides of Eq. (S3) (for constant values of k_1 and k_2) and rearranging the terms, we have,

$$\xi_i = \left(-\frac{1}{k_2} \ln \left(\frac{FMC(l_i, t)}{k_3(t)} \right) \right)^{\frac{1}{k_1}} \quad (\text{S5})$$

Using Eq. (S1) in (S5) we have,

$$l_i = \frac{l_D w_D}{w_i (k_2)^{\frac{1}{k_1}}} \left(-\ln \left(\frac{FMC(l_i, t)}{k_3(t)} \right) \right)^{\frac{1}{k_1}} \quad (\text{S6})$$

By taking derivative with respect to time on either side of Eq.(S6) we have,

$$\frac{d}{dt} \left(\ln \left(\frac{FMC(l_i, t)}{k_3(t)} \right) \right) = 0 \quad (\text{S7})$$

Using properties of natural logarithm and its derivative and using Eq.(S2), we have,

$$\frac{1}{k_3(t)} \frac{d}{dt} (k_3(t)) = \frac{1}{FMC(l_i, t) C_{\max}} \frac{d}{dt} (C(l_i, t)) \quad (\text{S8})$$

Or,

$$\frac{1}{k_3(t)} \frac{d}{dt} (k_3(t)) = \frac{J(l_i, t)}{FMC(l_i, t) C_{\max}} \quad (\text{S9})$$

where $J(l_i, t)$ is the rate of change of SMI concentration $C(l_i, t)$, and represents a reaction flux term at that location

$$J(l_i, t) = \frac{dC(l_i, t)}{dt} \quad (\text{S10})$$

Rearranging Eq (S11)

$$FMC(l_i, t) = \frac{J(l_i, t)k_3(t)}{C_{\max}} \frac{1}{\frac{d}{dt}(k_3(t))} \quad (S11)$$

Equation (S6) describes the length of the dendrite from the tip to the i^{th} point. From the definition of the length of the microdomain, as described in Section I, we can rewrite Eq.(S6) at $l_i = l_{md}$ as

$$l_{md} = \frac{l_D w_D}{w_{md} (k_2)^{\frac{1}{k_1}}} \left(-\ln \left(\frac{FMC(l_{md}, t)}{k_3(t)} \right) \right)^{\frac{1}{k_1}} \text{ where } FMC(l_{md}, t) = th_{COL_md} \quad (S12)$$

and w_{md} is the width of the dendrite at the corresponding length of l_{md} .

By taking derivative with respect to time on either side of Eq. (S12) and using the property that

$$l_{md} = \frac{w_{md}}{2} \tan \theta, \text{ the rate of change of the length of the microdomain is given by}$$

$$\frac{dl_{md}}{dt} = \left(\frac{l_D w_D}{2 w_{md}} \right) \frac{1}{(k_2)^{\frac{1}{k_1}}} \left(\frac{d}{dt} \left(-\ln \left(\frac{FMC(l_{md}, t)}{k_3(t)} \right) \right)^{\frac{1}{k_1}} \right) \text{ where } FMC(l_{md}, t) = th_{COL_md} \quad (S13)$$

Using Eq.(S11) and Eq.(S4) in Eq.(S13) and using the definition of length of the microdomain, we have the rate of change of l_{md} can be described by,

$$\frac{dl_{md}}{dt} = \frac{l_D w_D}{2 w_{md} (k_2)^{\frac{1}{k_1}}} \frac{d}{dt} \left(-\ln \left(\frac{J(l_{md}, t)}{\frac{d}{dt}(C_{\max_t})} \right) \right)^{\frac{1}{k_1}} \quad (S14)$$

$$\text{and } \frac{d}{dt} (C_{\max_t}) \neq 0$$

This analysis shows that the rate of change of the length of the microdomain is proportional to the combined effect of the width of the dendrite and natural log value of the rate of change of concentration of SMI.

Again, Eq.(S14) can be rewritten as,

$$\frac{dl_{md}}{dt} = s_{md} \frac{d}{dt} \left(-\frac{1}{k_2} \ln(\tilde{J}(l_{md}, t)) \right)^{\frac{1}{k_1}} \quad (S15)$$

where,

$$s_{md} = \frac{l_D w_D}{2w_{md}} = \frac{\text{area of the dendrite}}{\text{width of the dendrite corresponding to length } l_{md}}$$

$$\text{and } \tilde{J}(l_{md}, t) = \frac{J(l_{md}, t)}{\frac{d}{dt}(C_{\max, t})}$$

This representation allows us to capture the change of the length of the microdomain in terms of both shape and concentration in a single equation.

In eq.(S15), the normalized reaction flux term for a particular SMI, $\tilde{J}(l_{md}, t)$, represents the balance between the rate of production (or activation) and degradation (or inactivation) of the signaling components in the network. Thus, Eq. (S15) can also be expressed as:

$$\frac{dl_{md}}{dt} = s_{md} \left[-\frac{d}{dt} \left(\frac{1}{k_2} \ln \left(\tilde{j}_+(l_{md}, t) - \tilde{j}_-(l_{md}, t) \right) \right)^{\frac{1}{k_1}} \right] \quad (\text{S16})$$

The terms \tilde{j}_+ and \tilde{j}_- denote the sum of the rates for the production and degradation of the signaling components in the network respectively.

Description of Simulations

For the initial simulations we used a neuronal geometry where β -adrenergic receptor, G_s and adenylyl cyclase were localized to the cell surface plasma membrane and the remaining components of the systems, cAMP, PDE4, the MAPK cascade consisting of b-Raf, MEK and MAPK, PTP and PP2A were freely diffusible entities in the cytoplasm (Fig 1A, upper panel). The simulations were run in *Virtual Cell*. We utilized rate constants from the biochemical literature and constrained input-output relationships with experiments in the literature and performed in our laboratory for this study (see Fig S1. and (S12)). Simulations were initiated by activation of receptor by isoproterenol and the gradient of signaling components formed was observed as a function of time and distance.

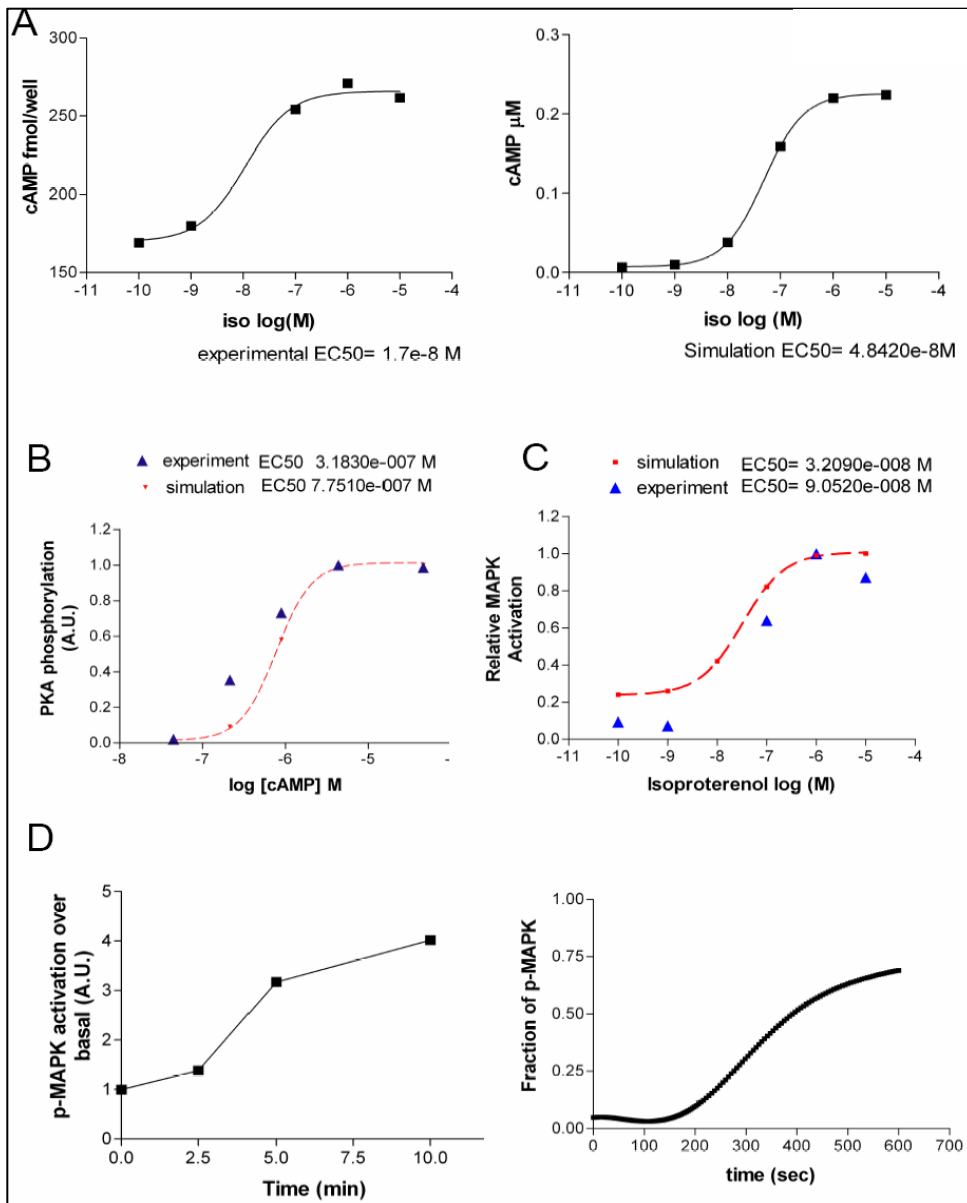


Fig S1. Experimental input/output relationships used to constrain the cAMP/MAPK model.

A. Effect of varying concentrations of isoproterenol on cAMP accumulation in hippocampal slices. Left - experimental dose response. Acute hippocampal slices were exposed to isoproterenol for 10 min in a submersion maintenance chambers with oxygenated ACSF. Right - Simulated dose response. B. Effect of varying concentrations of isoproterenol on PKA activation. Experimental data from (S13) C. Effect of varying concentrations of isoproterenol on MAPK activation. Acute hippocampal slices were exposed to isoproterenol for 10 min in a submersion maintenance chambers with oxygenated ACSF. D. Timecourse of Isoproterenol- dependent MAPK activation. Left - Acute hippocampal slices were exposed to isoproterenol (10 μ M) in a submersion maintenance chambers with oxygenated ACSF for indicated time points. Right - Simulated time course.

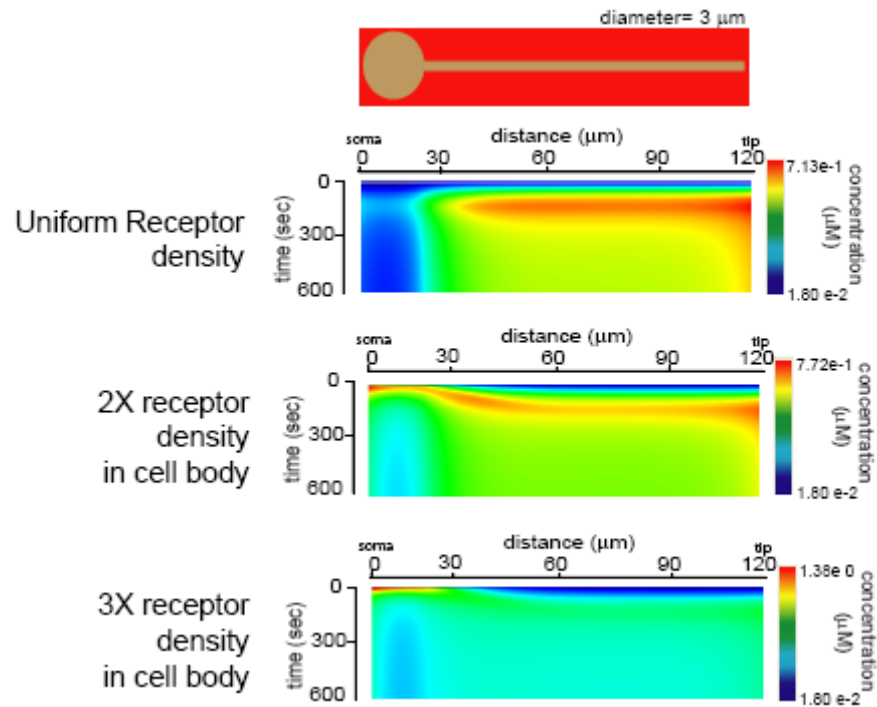


Fig S2 Increasing receptor density in cell body compensates for surface to volume effect on cAMP microdomains. cAMP kymographs of simulations where receptor density was increased from 94 molecules per μm^2 to 200 molecules per μm^2 (2X) and 300 molecules per μm^2 (3X). Geometry with a dendritic diameter of 3 μm was used

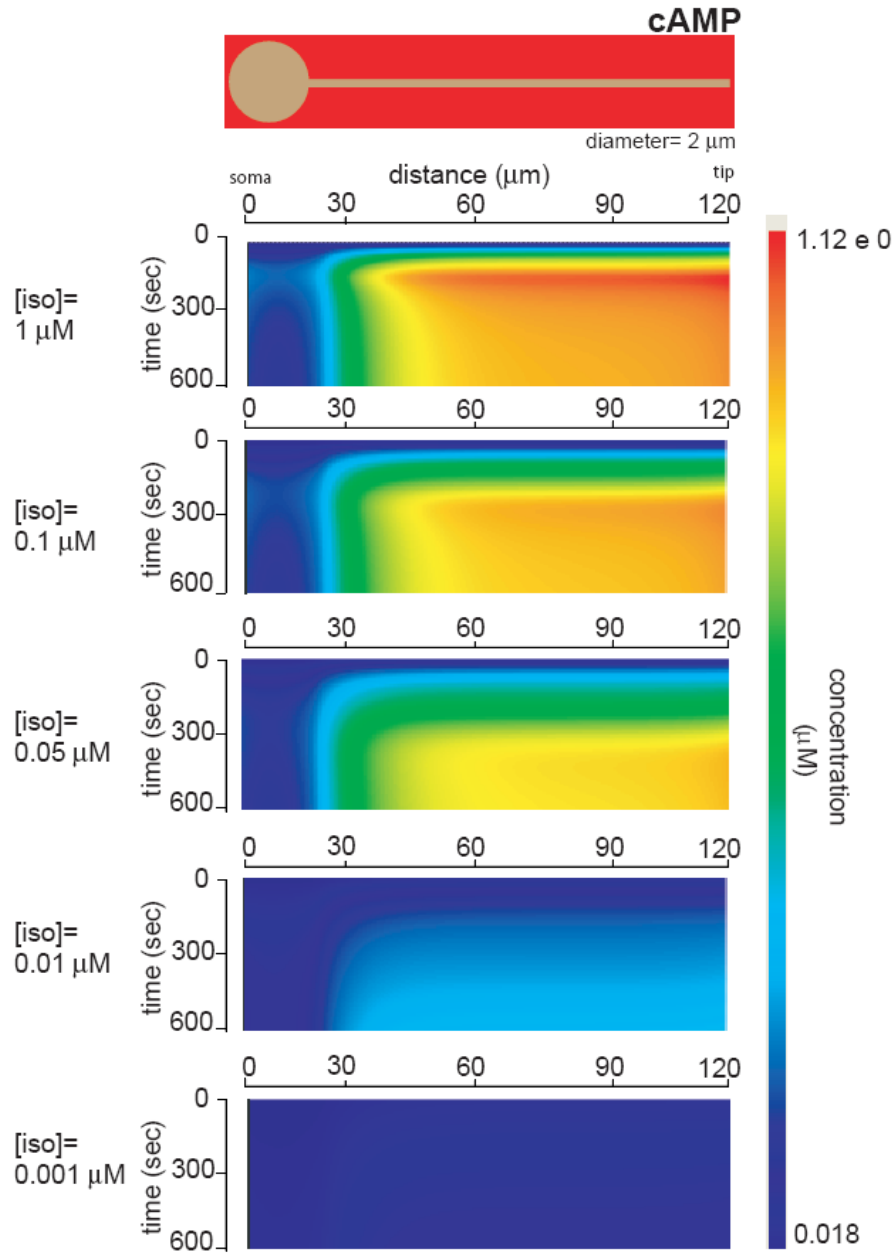


Figure S3 Effect of receptor occupancy on cAMP spatial domains. cAMP gradient in response to increasing isoproterenol concentrations. Isoproterenol was ranged from 0.001 to 1 μM. Geometry with a dendritic diameter of 2 μm was used.

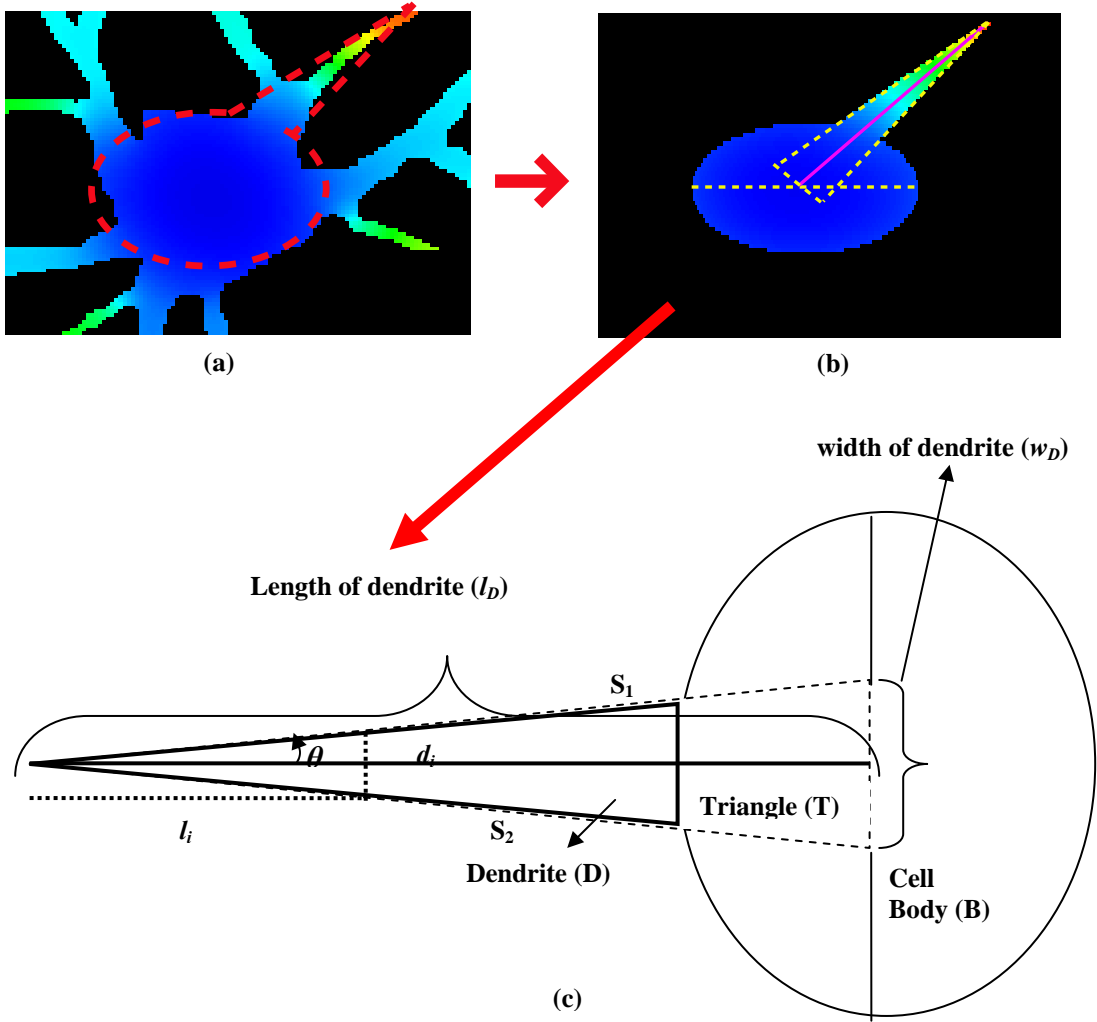


Figure S4. Conversion of neuronal shape from real to simplified geometry for mathematical analysis. Microdomains of cAMP in (a) neuronal geometry and (b) simplified geometry of the neuron containing an elliptical cell body and triangular dendrite. All simulation conditions were kept constant, and the numerical simulations were run in the finite volume solver. For both geometries, cAMP levels are shown for 600 s simulation time. (c) Schematic diagram of simplified neuron with one triangular dendrite (D) and elliptical cell body (S). We represent the membrane of the dendrite as two sides of a triangle (S_1 and S_2) and the cell body as an elliptical geometry. We extend the triangle (T) inside the elliptical cell body in order to compare the rate of production of a particular component, between the tip of the dendrite and near the central region of the cell body. l_D is the length of the extended dendrite i.e., length from the tip of the dendrite to the interior of the cell body. $l = 0$ implies the tip of the dendrite. w_D is the width of the extended dendrite, i.e., base of the triangle with sides S_1 and S_2 . l_i represents the length from the tip of the dendrite at the i^{th} point and w_i represents the corresponding width of the dendrite and is calculated as the base of the triangle made by the sides S_1 and S_2 at i^{th} point and normal to l_i .

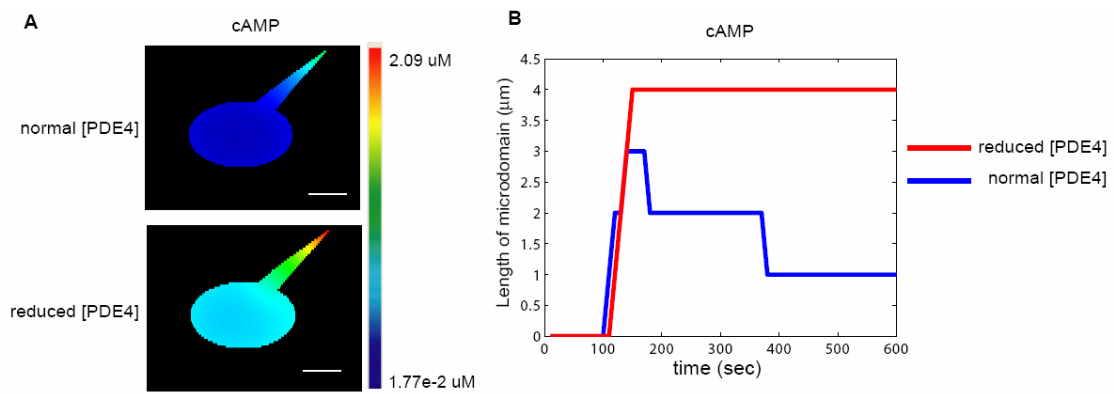


Figure S5. Relationship of the length of microdomains to normal and reduced PDE4 concentration in models of neurons with simplified geometries. The rate of change of length of the microdomain, based on the calculation of l_{md} , as depicted in the equation 1, is shown for cAMP in (B). (A) shows the color-coded spatial distribution of cAMP, with normal phosphodiesterase concentration (top) or reduced phosphodiesterase concentration (bottom) at 10 mins. (B) shows the change of l_{md} with time for cAMP, with normal or reduced phosphodiesterase concentrations.

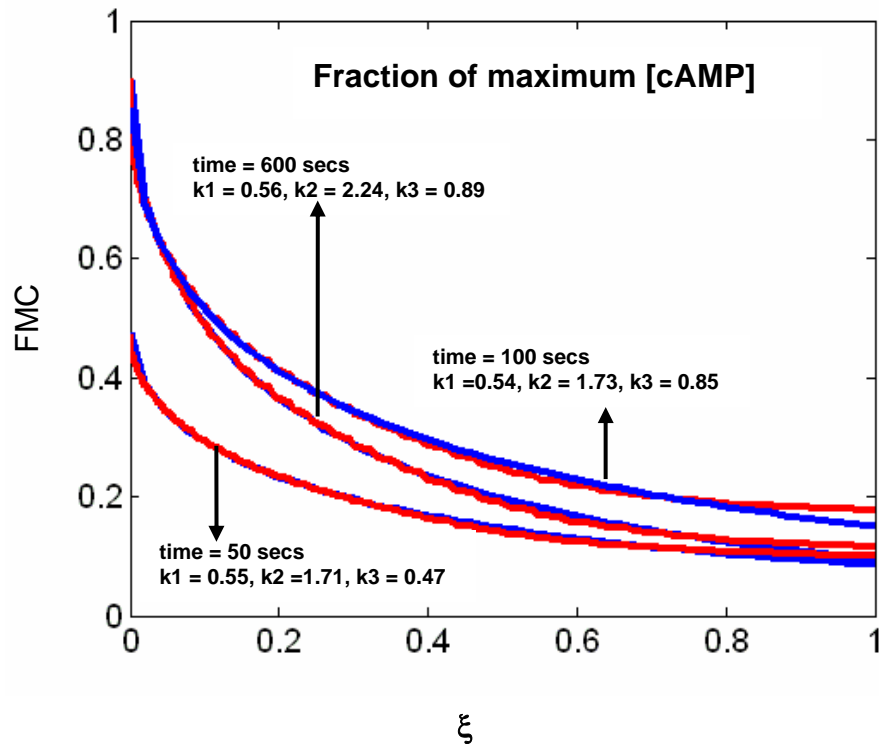


Figure S6. The change of FMC with the normalized length ξ for fraction of maximum [cAMP] at different times. The red curves are the results obtained from the numerical simulations and the blue curves are the fitted curves from equation S3.

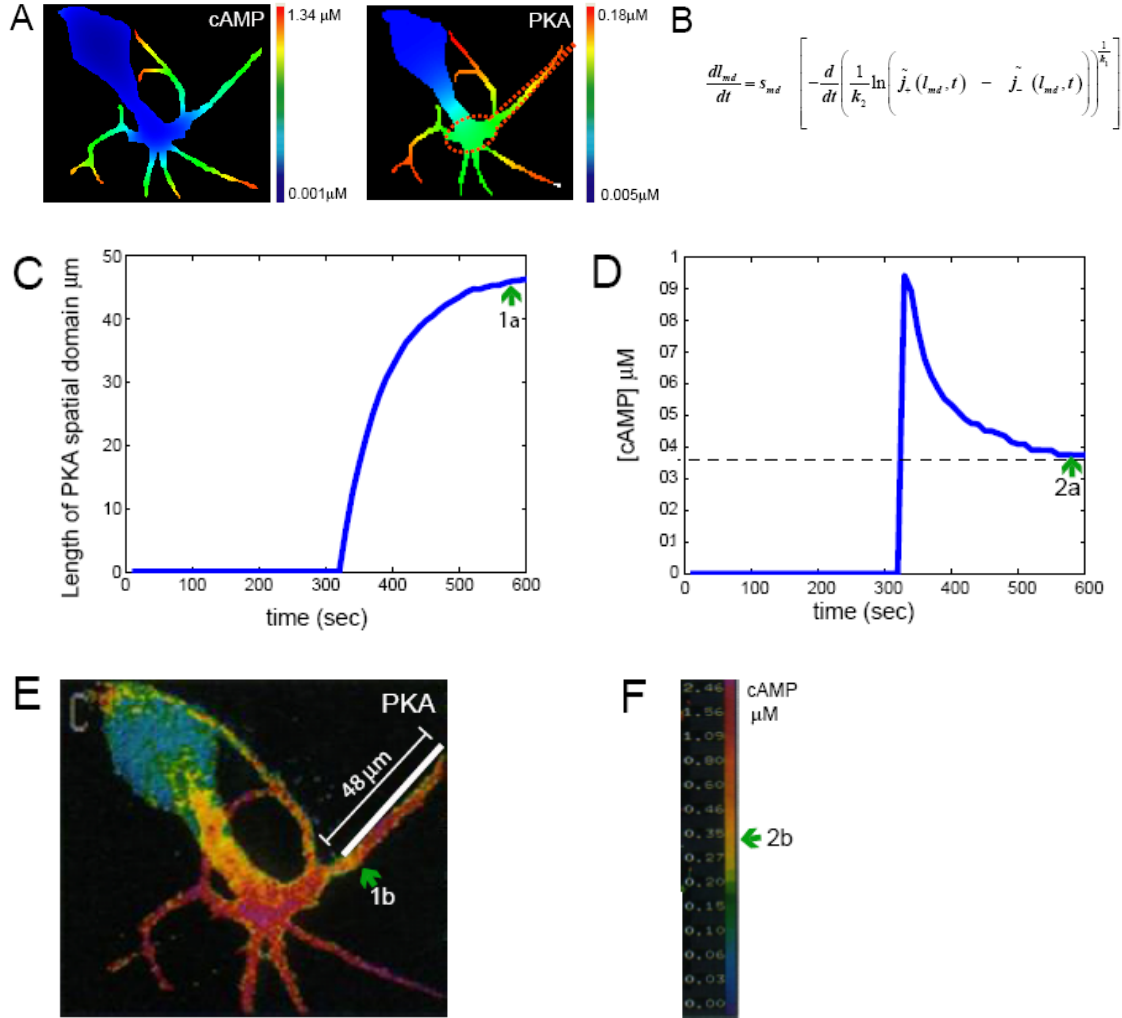


Fig S7 Use of mathematical representation to compare the cAMP spatial model to experimental data

(A) Simulated cAMP (left panel) and PKA gradients (right panel) in response to stimulus of an Aplysia neuron in culture, as shown in ref. (10). Since the concentrations of the signaling components in the Gs-cAMP pathway in Aplysia are not known, we used values for the mammalian β -adrenergic pathway. The temporal characteristics of cAMP generation, and PKA activation are likely to differ, and no attempt was made to match them. We compared the experimental data with our simulations at a time point where the microdomain length approaches maximal (600 s, denoted by arrows 1a and 2a). The red dashed outline indicates the dendrite used in the analysis. This dendrite was selected since in the original image (see S7E) is the only non overlapping dendrite. (B) Equation used to estimate the length of the microdomain, l_{md} . $j(l_{sd}, t)$ is the rate of change of a signaling component normalized by the rate of change of the maximum concentration of the component along the axis of measurement, at a particular time. The subscripts '+' and '-' denote the sum of the rates for the production and degradation of the signaling components in the network. The axis of measurement was sampled at discrete points termed i^{th} . The length, l_{sd} , is defined by threshold (th_{COL_md}), such that the concentration of a component from the origin (or tip of the dendrite) to the i^{th} point on the length of the dendrite, $C(l_i, t)$, is described by $C(l_i, t) \geq th_{COL_md} * C_{max}$. This holds for all $l_i \leq l_{md}$ at all time t, where $0 \leq th_{COL_sd} \leq 1$. C_{max} is the maximum concentration of a signaling component along the projected length of the dendrite at all times. S_{md} (cell shape factor) is the ratio of the area of the dendrite and the width of the dendrite corresponding to length l_{md} . k_1 (production parameter) and k_2 (degradation parameter) were values obtained from the curve fitting. (C) Change of length of microdomain with time, based on calculation of l_{md} for PKA using equation 1. Green arrow labeled 1a represents the distance of the PKA microdomain at 600 sec. (D) cAMP concentrations obtained from simulation as a function of time corresponding to the lengths of the PKA microdomains shown in fig S7C. Green arrow

labeled 2a indicates cAMP concentration at 600 sec at the length specified in S7B as indicated by arrow 1a. (E) Experimental measurements of PKA activation by FRET from (10). On this image we used the calculated l_m of 48 μm from the tip of the dendrite towards the cell body to identify the boundary of the microdomain which is marked by green arrow 1b. (F) We then used the color scale for cAMP provided in (10)) to estimate the cAMP concentration at point 1b. The estimated concentration of cAMP by comparison of the color scale indicates a value of about 0.33 μM as shown by the green arrow 2b. This value is in agreement with the value of 0.35 μM obtained in numerical simulation, as indicated by arrow 2a in S7D.

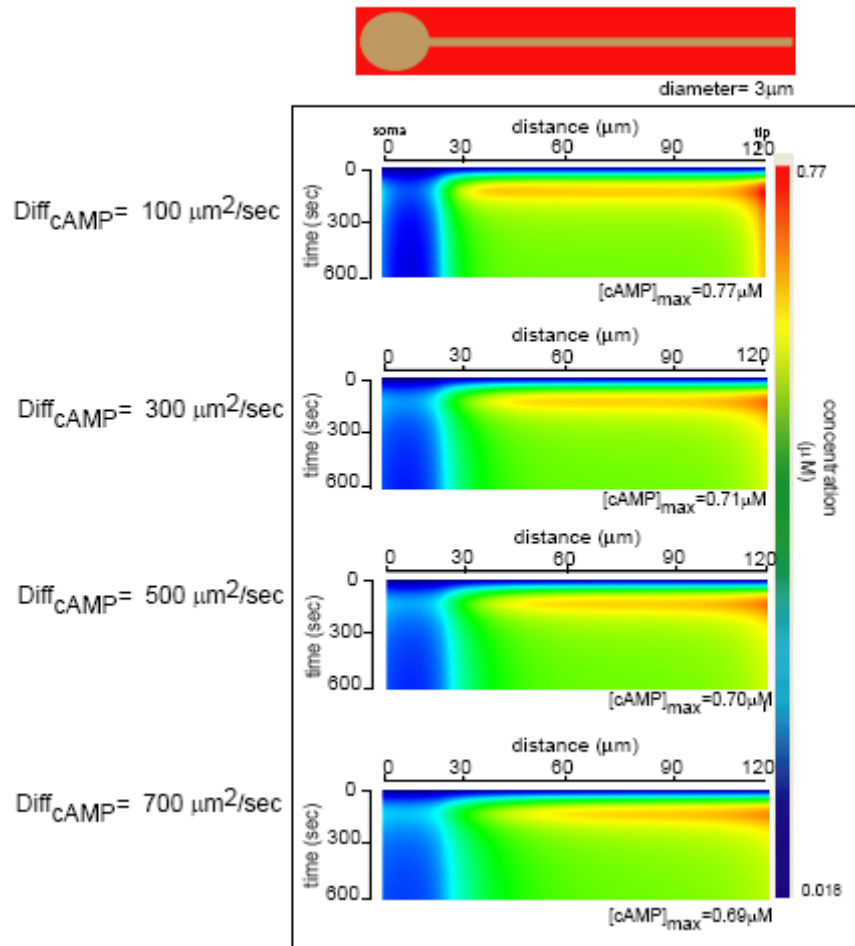


Figure S8. Varying the cAMP diffusion coefficient has little effect on the cAMP microdomains. The cAMP diffusion coefficient values of 100, 300, 500 and 700 $\mu\text{m}^2/\text{s}$ were tested. The cAMP diffusion coefficient used in the present study was 300 $\mu\text{m}^2/\text{s}$ (S3). Values tested are based on experimentally measured diffusion coefficients 500 $\mu\text{m}^2/\text{s}$ (S14) and 700 $\mu\text{m}^2/\text{s}$ (S10).

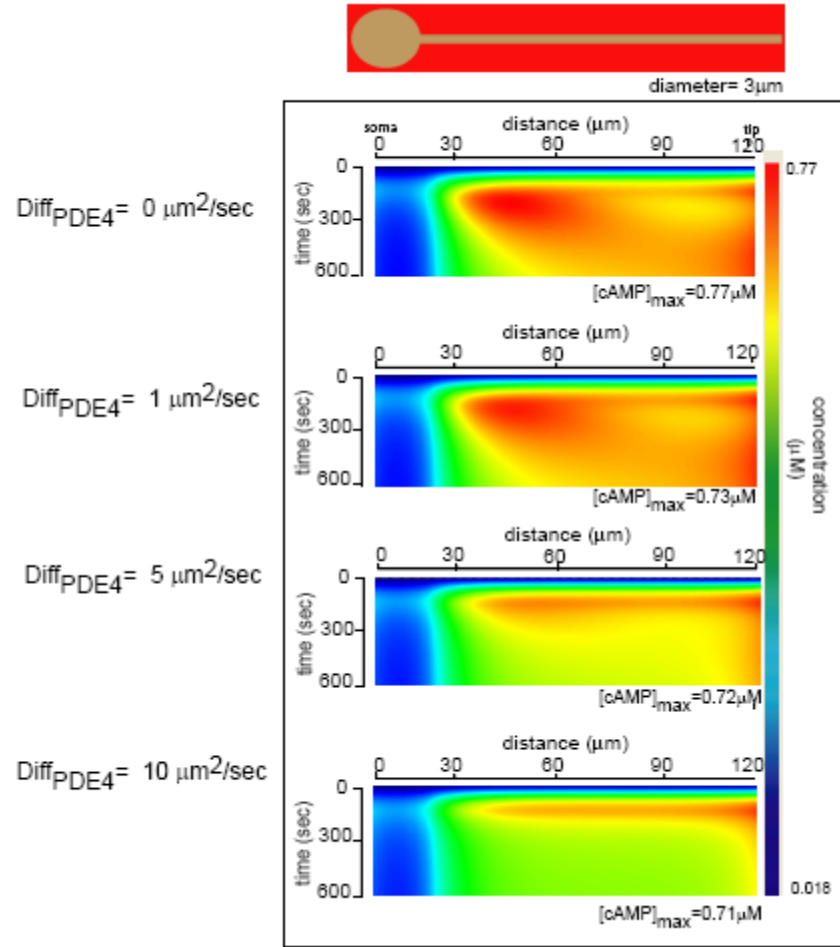


Figure S9. Varying the PDE4 diffusion coefficient changes the dynamics of cAMP microdomain. The PDE4 diffusion coefficient used in this study was $5\mu\text{m}^2/\text{s}$, and this value was calculated based on PDE4 molecular weight.

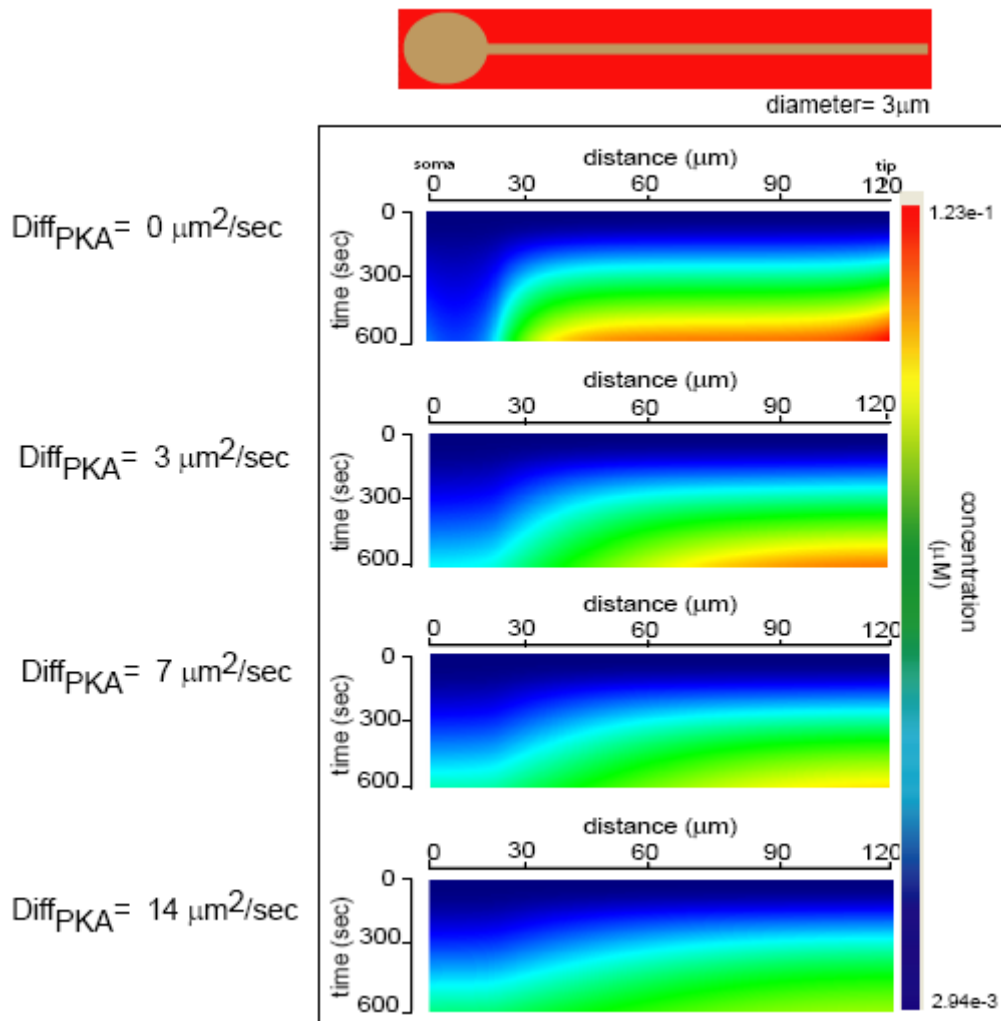


Figure S10. Varying the PKA diffusion coefficient has little effect on the dynamics of PKA microdomain. The PKA diffusion coefficient used in this study was $3 \mu\text{m}^2/\text{s}$, and this value was calculated based on PKA molecular weight.

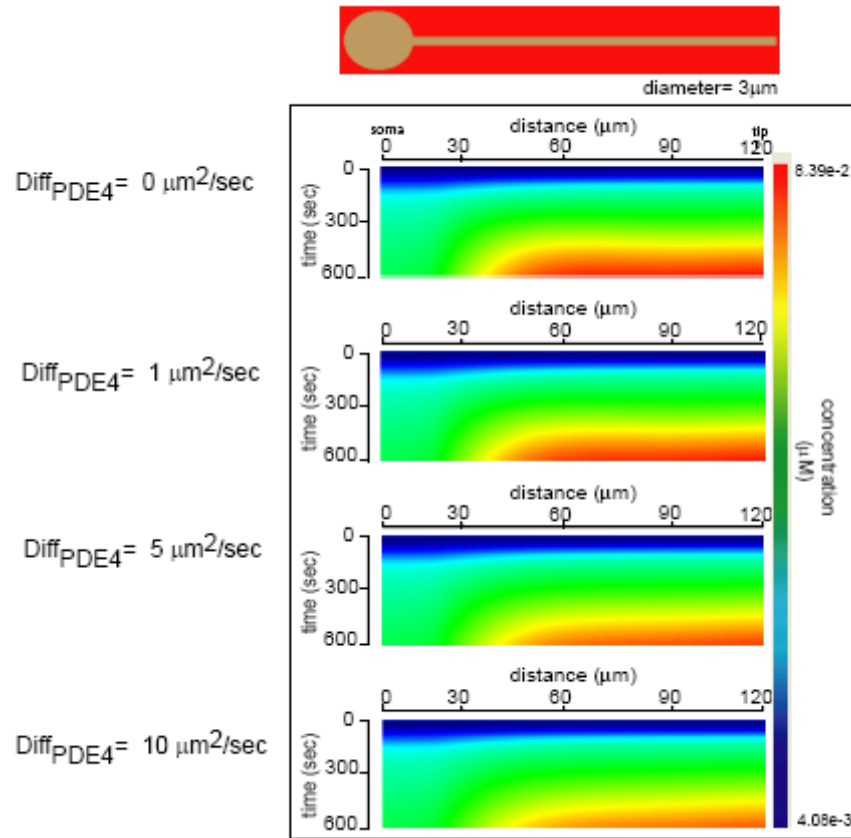


Figure S11. Changing the PDE4 diffusion coefficient has little effect on the MAPK microdomain. The PDE4 diffusion coefficient used in this study was $5 \mu\text{m}^2/\text{s}$, and this value was calculated based on PDE4 molecular weight.

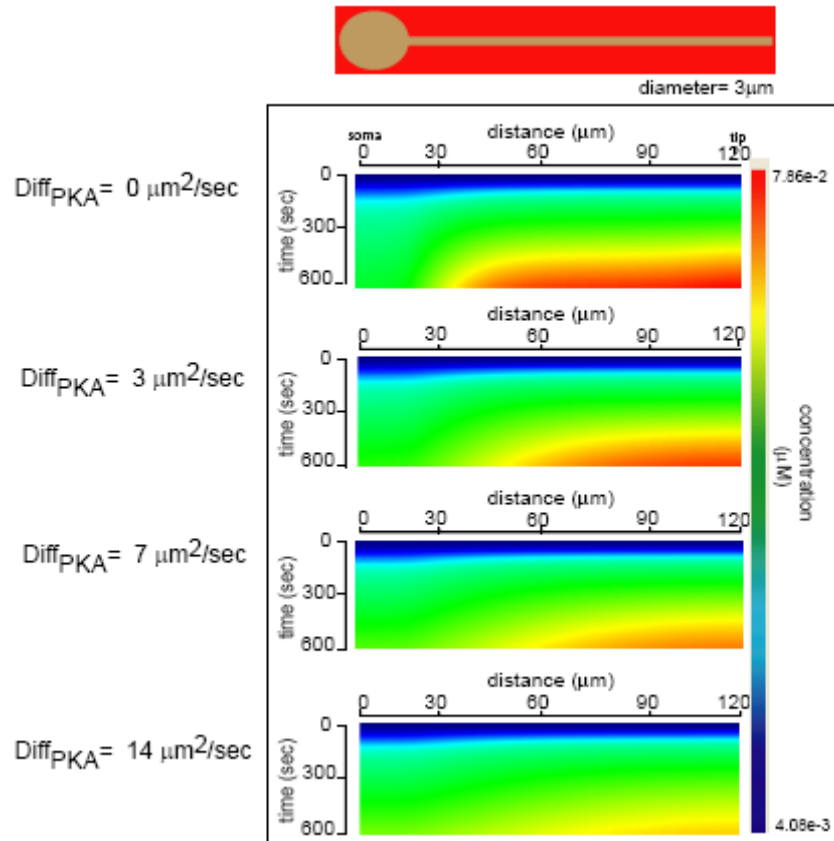


Figure S12. Varying the PKA diffusion coefficient has little effect on the MAPK microdomain. The PKA diffusion coefficient used in this study was 3 $\mu\text{m}^2/\text{s}$, and this value was calculated based on PKA molecular weight.

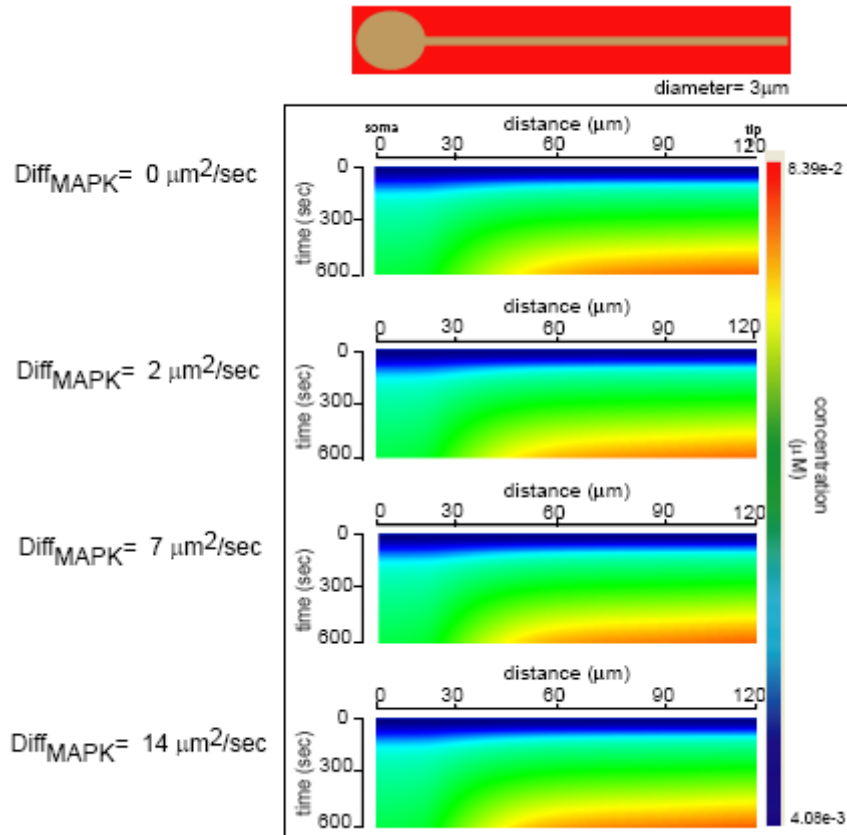


Figure S13. Varying the MAPK diffusion coefficient has little effect on the MAPK microdomain. The MAPK diffusion coefficient used in this study was $7 \mu\text{m}^2/\text{s}$, and this value was calculated based on MAPK molecular weight.

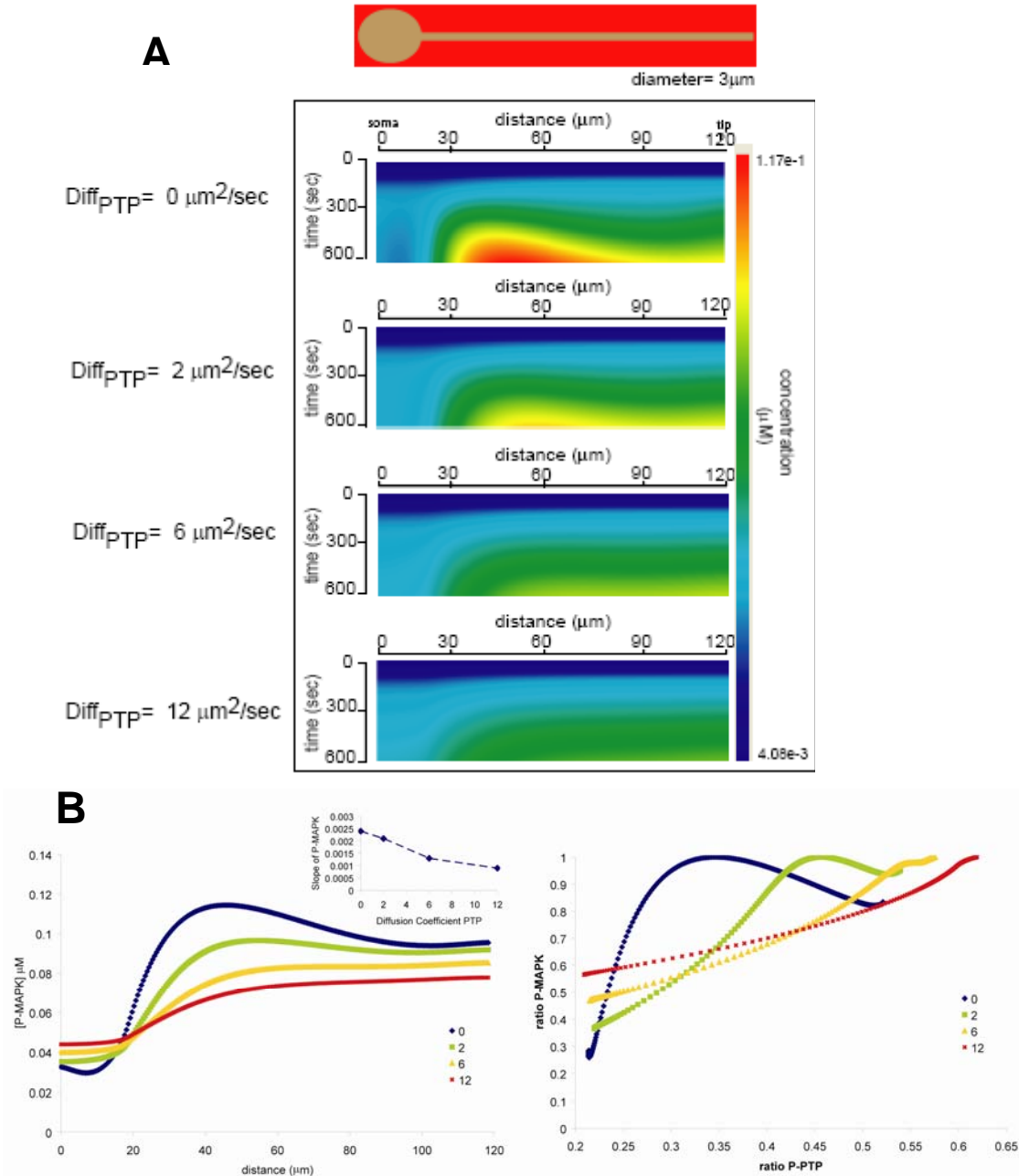


Figure S14. Varying the PTP diffusion coefficient affects the MAPK microdomain. (A) Kymographs of P-MAPK gradients with varying PTP diffusion coefficients. The PTP diffusion coefficient used in this study was $6 \mu\text{m}^2/\text{s}$, and this value was calculated based on PTP molecular weight. (B) left panel- corresponding spatial gradient line plot of P-MAPK at 600 sec over the length of the geometry (0 μm cell body, 120 μm tip of dendrite) with varying PTP diffusion coefficients. (inset) plot of the slope of the linear range (20-40 μm) of the P-MAPK gradient as a function of PTP diffusion coefficients. Right panel- Ratio of P-MAPK to maximal P-MAPK as a function of ratio of P-PTP to total PTP with varying PTP diffusion coefficients.

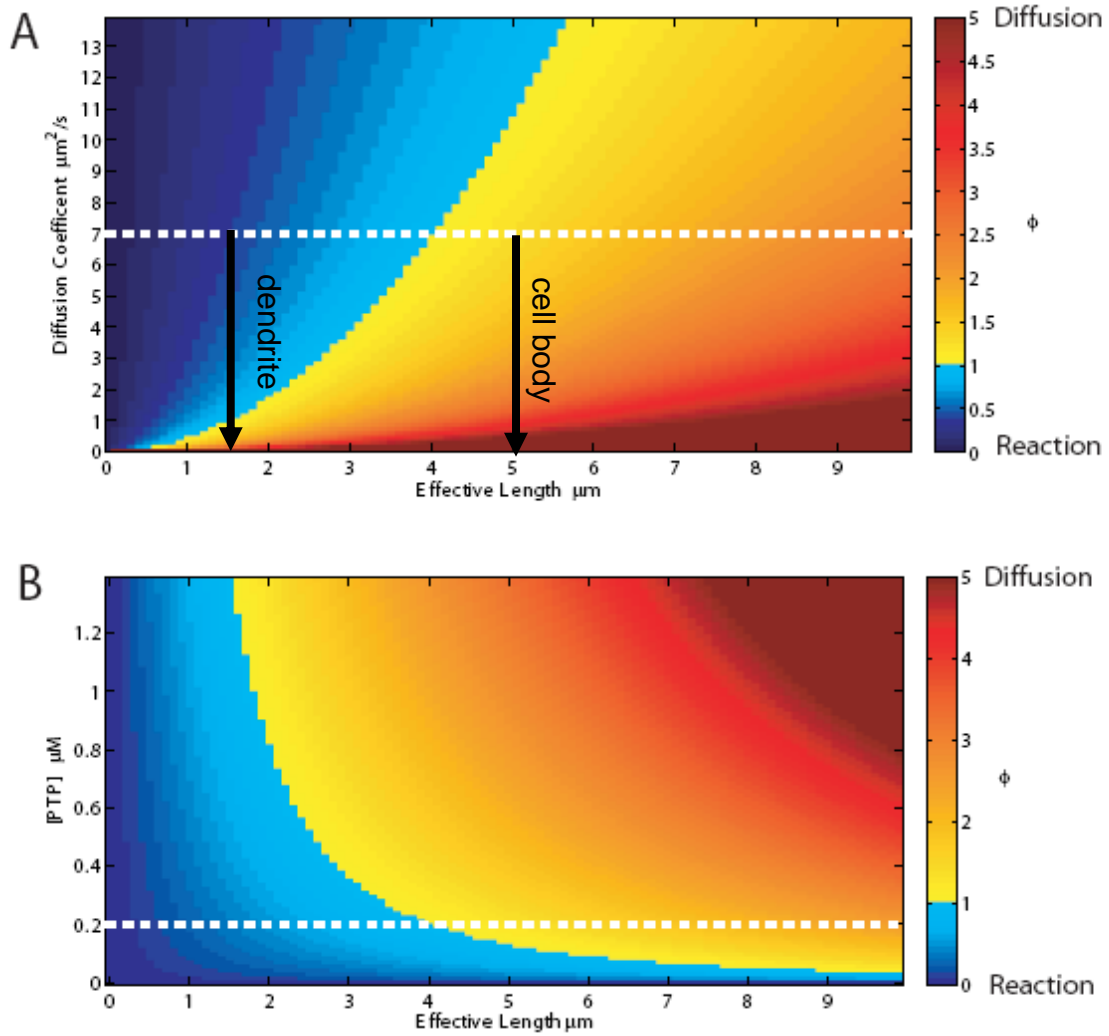


Figure S15. Effect of varying effective length on P-MAPK Thiele modulus ϕ (A) ϕ was calculated over a range of effective length values (L_{eff}) and diffusion coefficient values for P-MAPK at a [PTP] of $0.2 \mu\text{M}$. The diffusion coefficient value used in the simulations is highlighted with a white dashed line. (B) ϕ was calculated over a range of effective length values (L_{eff}) and PTP concentration values for P-MAPK, while MAPK diffusion coefficient was $7 \mu\text{m}^2/\text{sec}$. The PTP concentration used in the simulations is highlighted with a white dashed line. For details see Table S6.

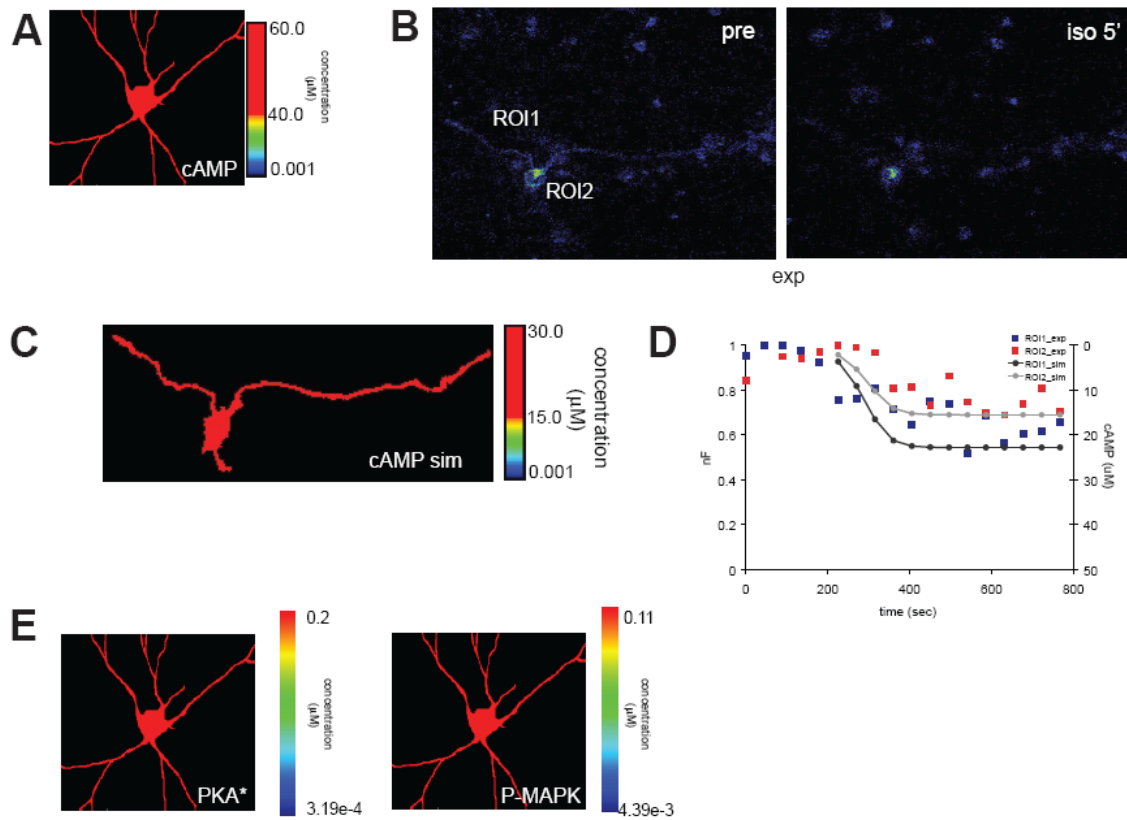


Figure S16. Effect of negative regulator PDE4 regulation on downstream microdomains. (A) Simulation of isoproterenol-stimulated cAMP formation in a neuron where PDE4 was reduced. (B) Dynamics of cAMP formation in live primary hippocampal neurons using the cAMP FRET sensor EPAC1 after pretreatment with rolipram for 30 min. The images show the calculated nF prior to addition of isoproterenol (10 μ M, left panel) and 5 minutes post addition (right panel). (C) Simulation of isoproterenol cAMP formation using neuronal shape from FRET experiment in 3B with PDE4 reduced. The scale has been set to appropriately compare with the dynamic range of the FRET probe. (D) Comparison of cAMP FRET at ROI1 (dendrite) and ROI2 (cell body) with simulation results in their corresponding locations. (E) Simulations of isoproterenol stimulated PKA (PKA*) and MAPK (P-MAPK) in PDE4 reduced neurons.

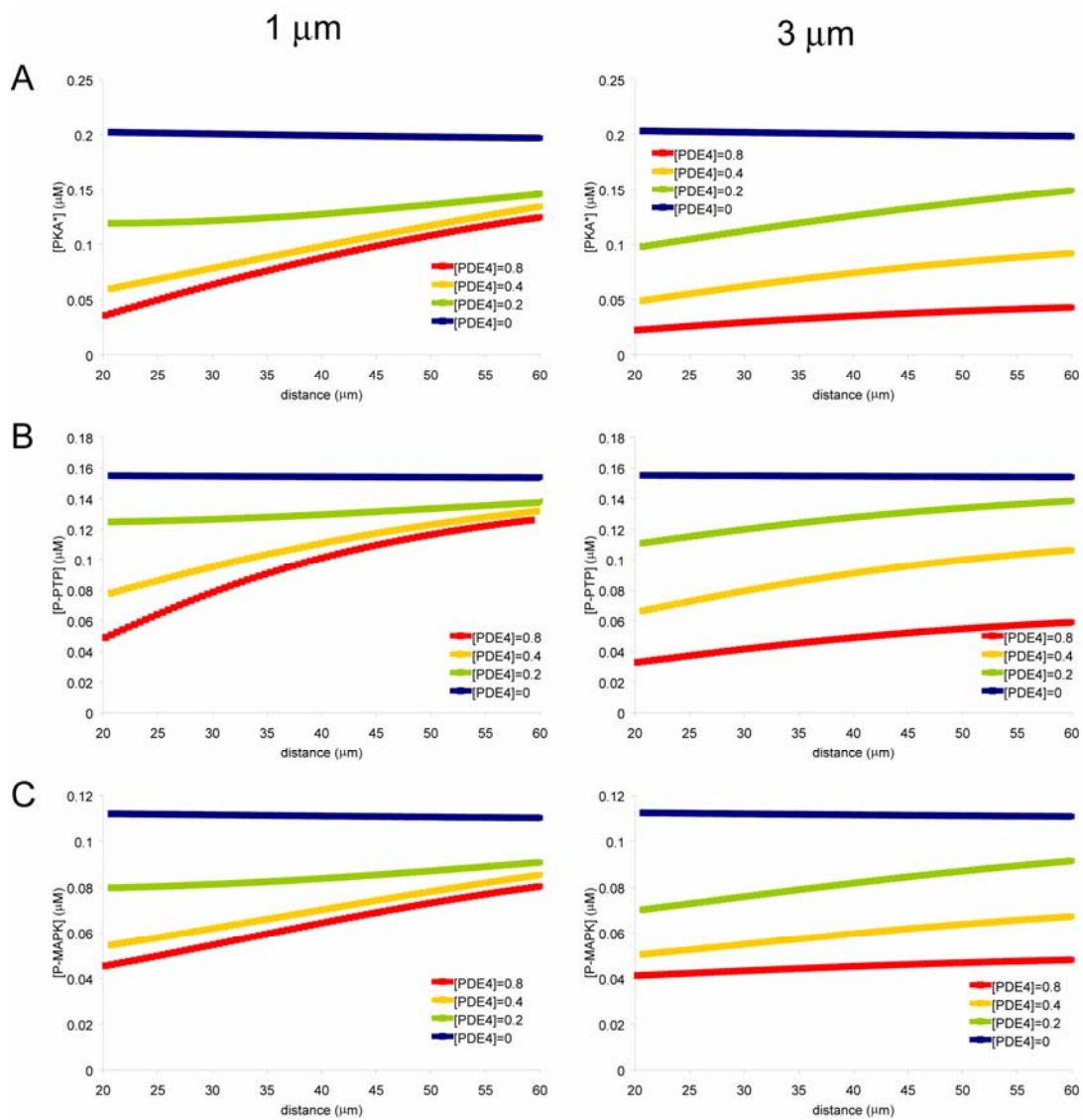


Figure S17. Plots of the linear range of the isoproterenol-induced gradients at 600 sec of activated PKA (A), P-PTP (B), and P-MAPK (C) for varying concentrations of PDE4. Gradients taken from the 1 and 3 μm dendritic diameter geometries shown in Fig 3.

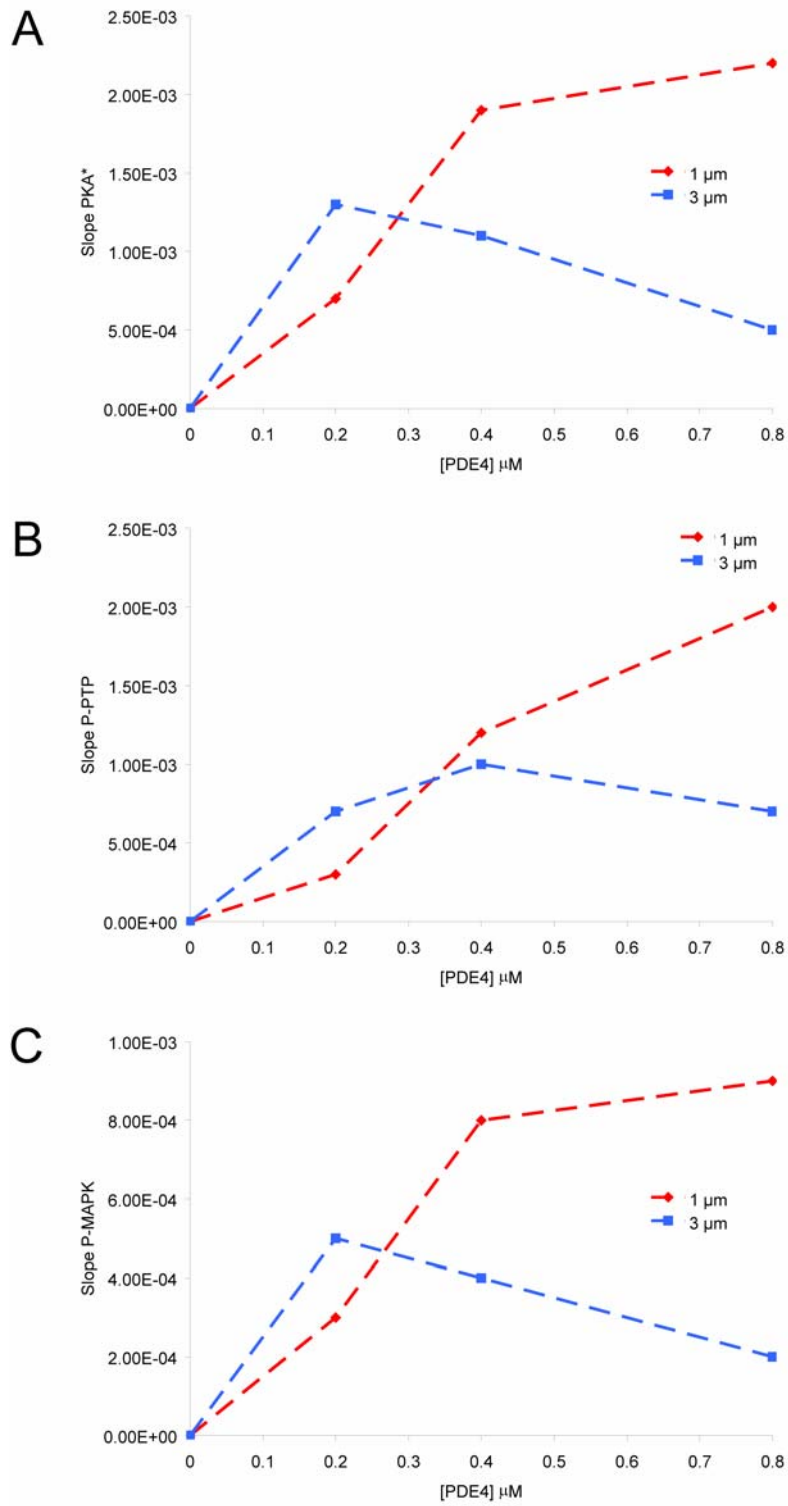


Figure S18 Dendritic diameter and PDE4 concentration determines the slope of the gradient for activated PKA (A), P-PTP (B) and P-MAPK (C). The slopes for the linear range of the gradients were calculated by linear regression.

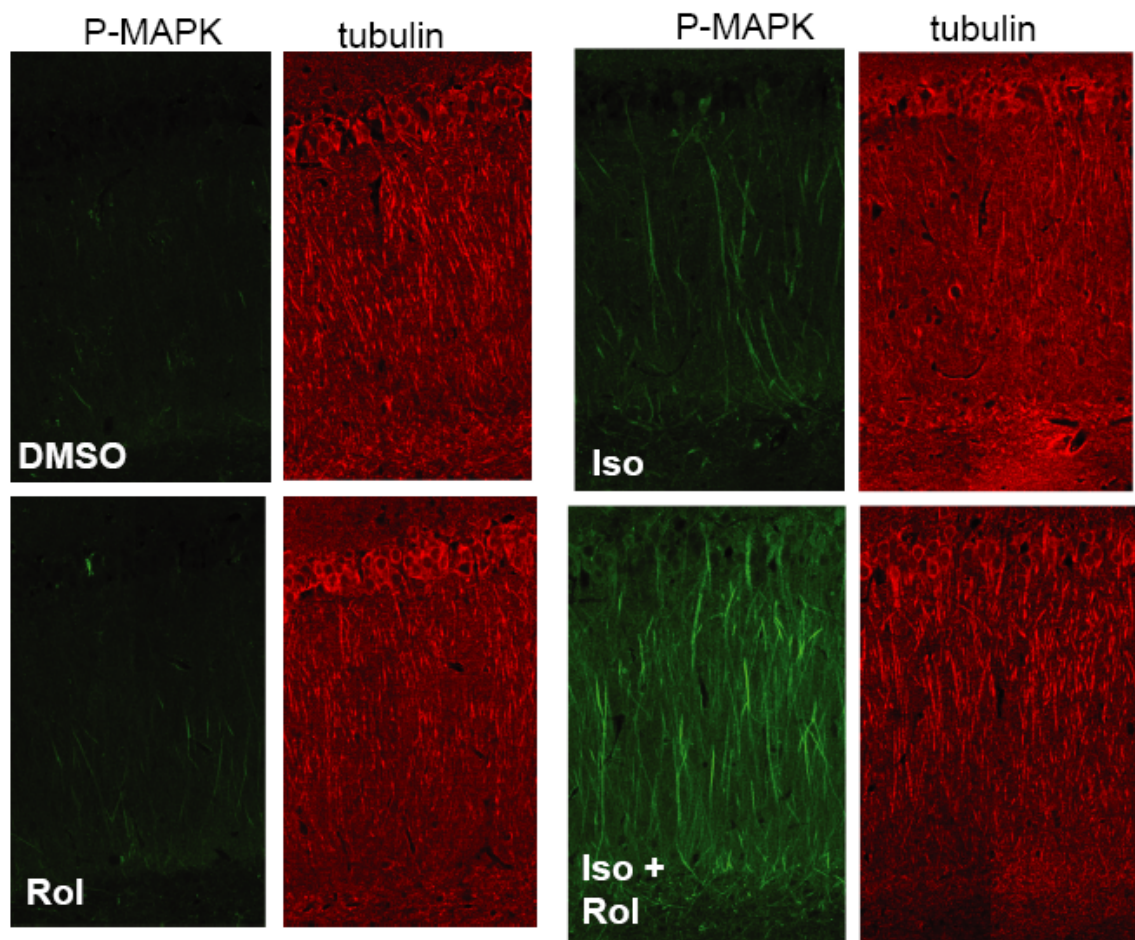


Figure S19 Effect of rolipram inhibition on isoproterenol- induced activation of MAPK. Confocal images of P-MAPK (green) and tubulin (red) immunofluorescence of CA1 hippocampal neurons in rat brain slices. Hippocampal slices were treated with vehicle (DMSO, top left), with 10 μ M rolipram (PDE4 inhibitor) for 30 min (Rol, bottom left), with 10 μ M isoproterenol for 20 min (Iso, top right) or with 10 μ M rolipram for 30 min followed by 10 μ M isoproterenol for 20 min (Iso +Rol, bottom right).

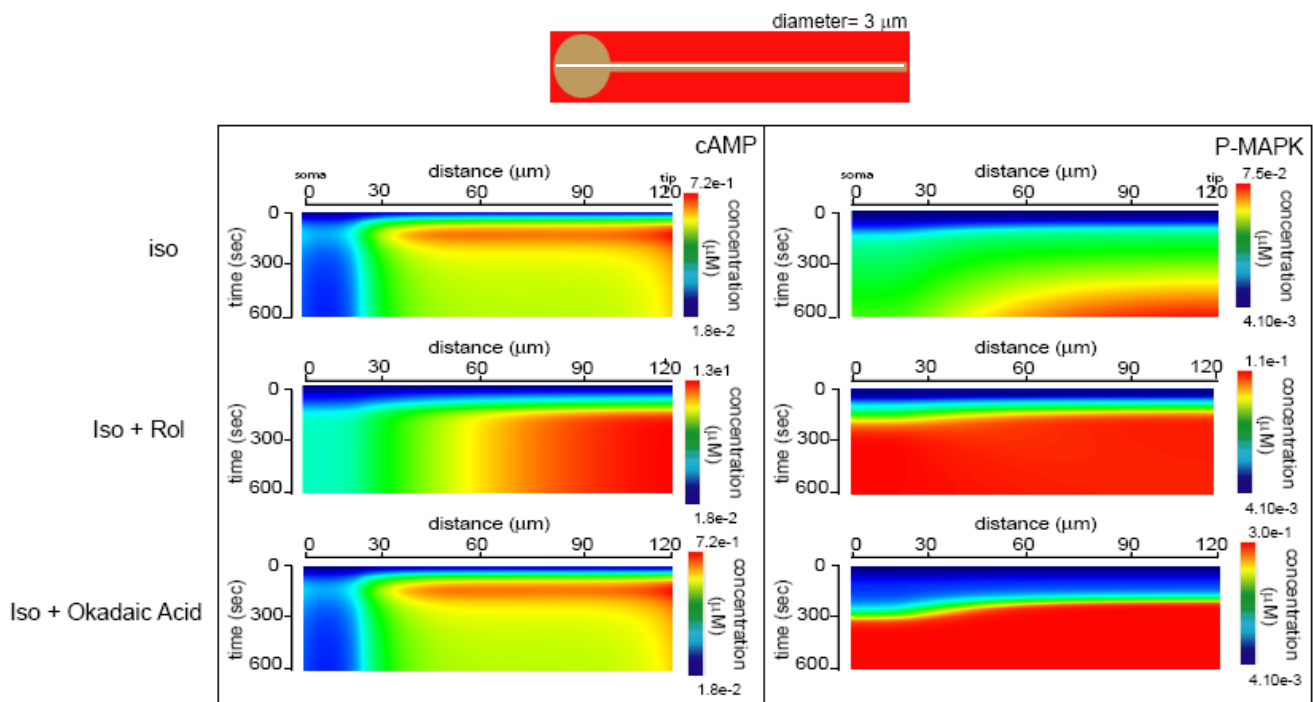


Figure S20. Comparison of the simulated cAMP and P-MAPK microdomains in isoproterenol-stimulated (iso), isoproterenol + rolipram (iso+rol), and isoproterenol +okadaic acid (Iso+ Okadaic Acid) inhibited neurons. Kymographs show cAMP (left) and P-MAPK (right) concentrations as a function of time and distance along a dendrite. Location is shown in the schematic at the top of the figure (white line).

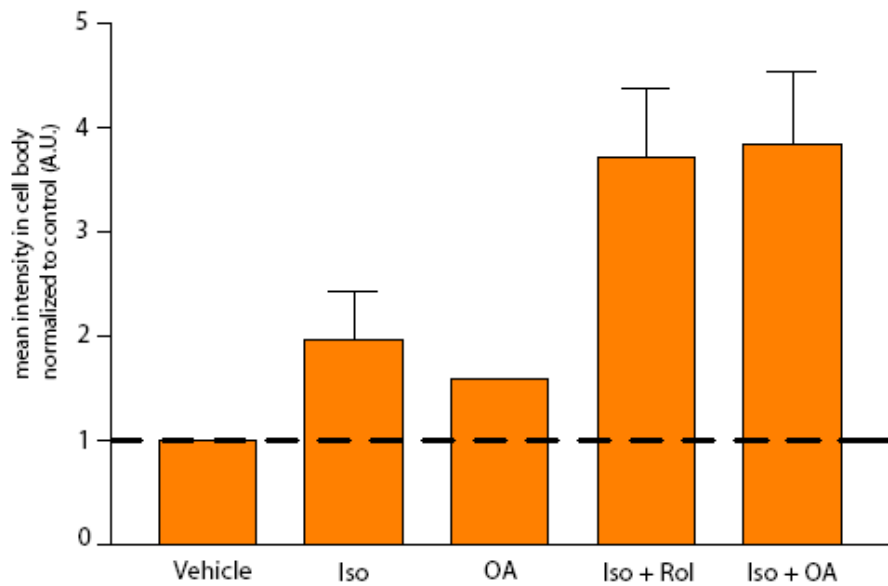
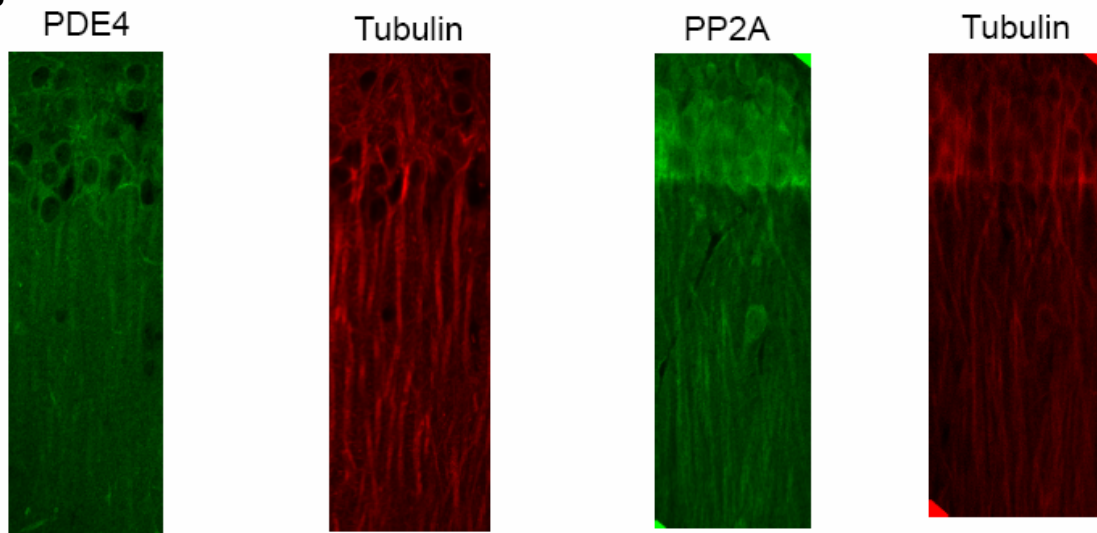
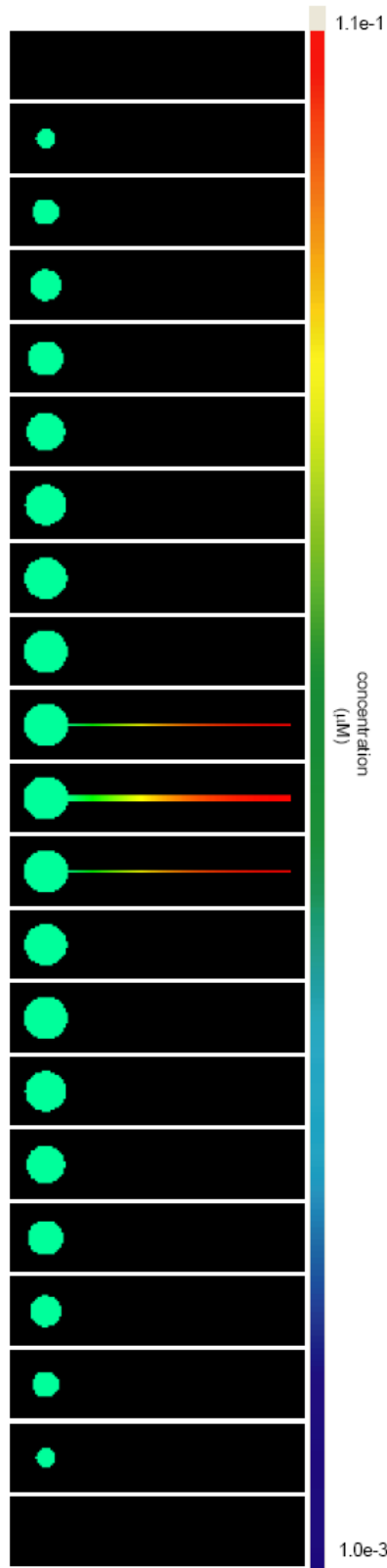
A**B**

Figure S21. Effect of inhibitors of the negative regulators PDE4 and PP2A on the phosphor-MAPK microdomains in hippocampal slices

(A) Hippocampal slices were treated with vehicle (DMSO), with 10 μ M isoproterenol for 20 min (iso), with 1 μ M okadaic acid for 30 min (oa), or with 10 μ M rolipram for 30 min followed by 10 μ M isoproterenol for 20 min (iso+rol), or with 1 μ M okadaic acid for 30 min followed by 10 μ M isoproterenol for 20 min (iso+oa). Quantification of mean intensity of immunoreactivity of P-MAPK in cell body region of CA1 neurons in all four conditions (n=3). Each experiment was normalized to DMSO control. (B) PDE4 and PP2A are uniformly distributed in cell bodies and dendrites of CA1 neurons. Immuno staining of PDE4 and PP2A and corresponding tubulin staining in CA1 neurons in hippocampal slices.

A



B



Fig S22 3-D spatial simulation of P-MAPK gradients upon global stimulation of beta-adrenergic receptor. (A) The cell body is considered a sphere and its dimensions are 20 μm in diameter. The dendrite is considered a cylinder with a length of 100 μm and a diameter of 2 μm .

(B) 2-D spatial simulation of P-MAPK gradients upon global stimulation of beta-adrenergic receptor using previously used geometry. In this geometry, the cell body is a circle with a diameter of 20 μm , and the dendrite is a rectangle with a length of 100 μm , and a width of 2 μm . For details see table S3.

To validate the comparison between the 2D and 3D models, we have calculated the surface to volume ratios for a circle/rectangle combination and sphere/cylinder combination and find that the ratios of cell body to dendrite in both cases are similar. The calculations are shown below:

To validate the comparison between the 2D and 3D models, we have calculated the surface to volume ratios for a circle/rectangle combination and sphere/cylinder combination and find that the ratios of cell body to dendrite in both cases are similar. The calculations are shown below:

2D

3D

| | |
|----------------------|--------------------------|
| Circle | Sphere |
| Circumference | Surface |
| $P = 2\pi R$ | $S = 4\pi R^2$ |
| Area | Volume |
| $A = \pi R^2$ | $V = \frac{4}{3}\pi R^3$ |
| $R = 10 \mu\text{m}$ | $R = 10 \mu\text{m}$ |
| $S/V_c = 0.2$ | $S/V_s = 0.3$ |

| | |
|-----------------------|--------------------------|
| Rectangle | Cylinder |
| Perimeter | Surface |
| $P = 2L + 2W$ | $S = 2\pi R^2 + 2\pi RH$ |
| Area | Volume |
| $A = L \times W$ | $V = \pi R^2 H$ |
| $W = 2 \mu\text{m}$ | $R = 1 \mu\text{m}$ |
| $L = 100 \mu\text{m}$ | $H = 100 \mu\text{m}$ |
| $S/V_r = 1.02$ | $S/V_{cy} = 2.02$ |

1.0e-3

Ratio S/V_c to $S/V_r = 0.20$ Ratio S/V_s to $S/V_{cy} = 0.15$

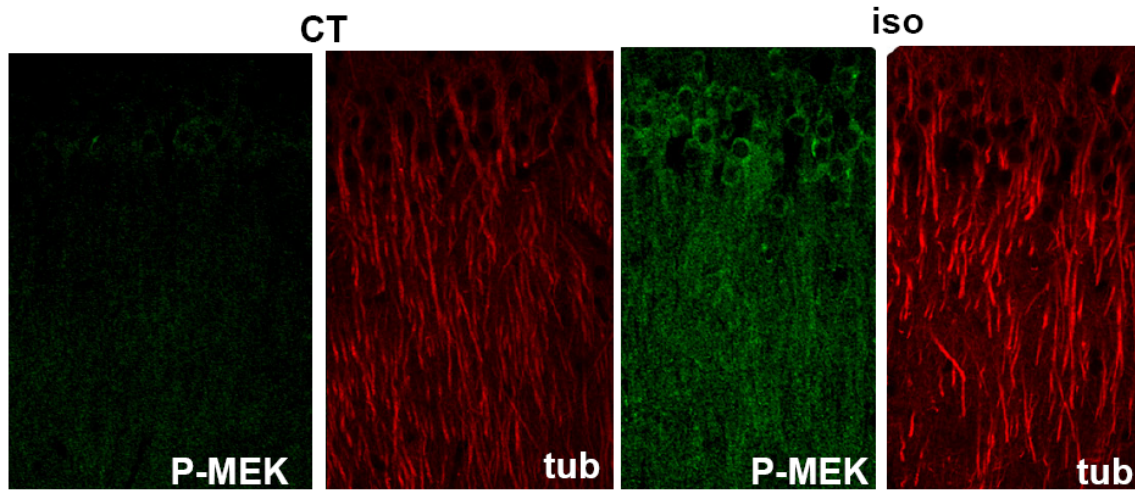


Figure S23. P-MEK distribution upon Isoproterenol-stimulation. Confocal images of P-MEK (green) and tubulin (red) immunofluorescence of CA1 hippocampal neurons. Hippocampal slices were treated with vehicle (CT, left), or with 10 μ M isoproterenol for 20 min (Iso, right), fixed and stained with P-MEK antibodies and visualized by confocal microscopy.

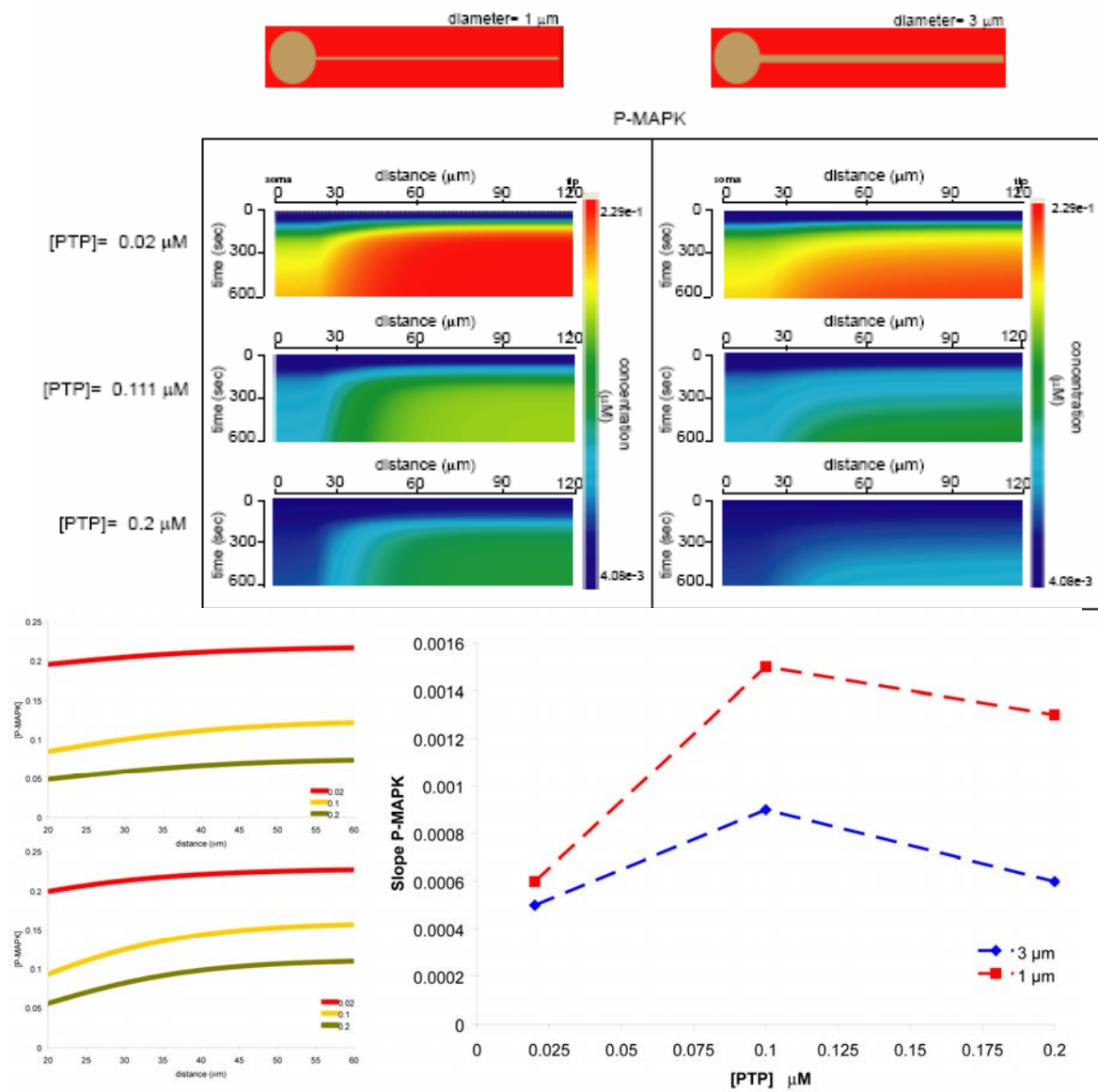


Figure S24 Effect of varying PTP concentration on P-MAPK microdomains. (top) Kymographs of P-MAPK concentration with respect to time and space for varying PTP concentration at 1 μm (left panel) and 3 μm (right panel) dendritic diameter. (bottom) Plots of the linear range of the isoproterenol-induced gradients of P-MAPK at 600 sec (left) and corresponding slopes (right) for varying concentrations of PTP.

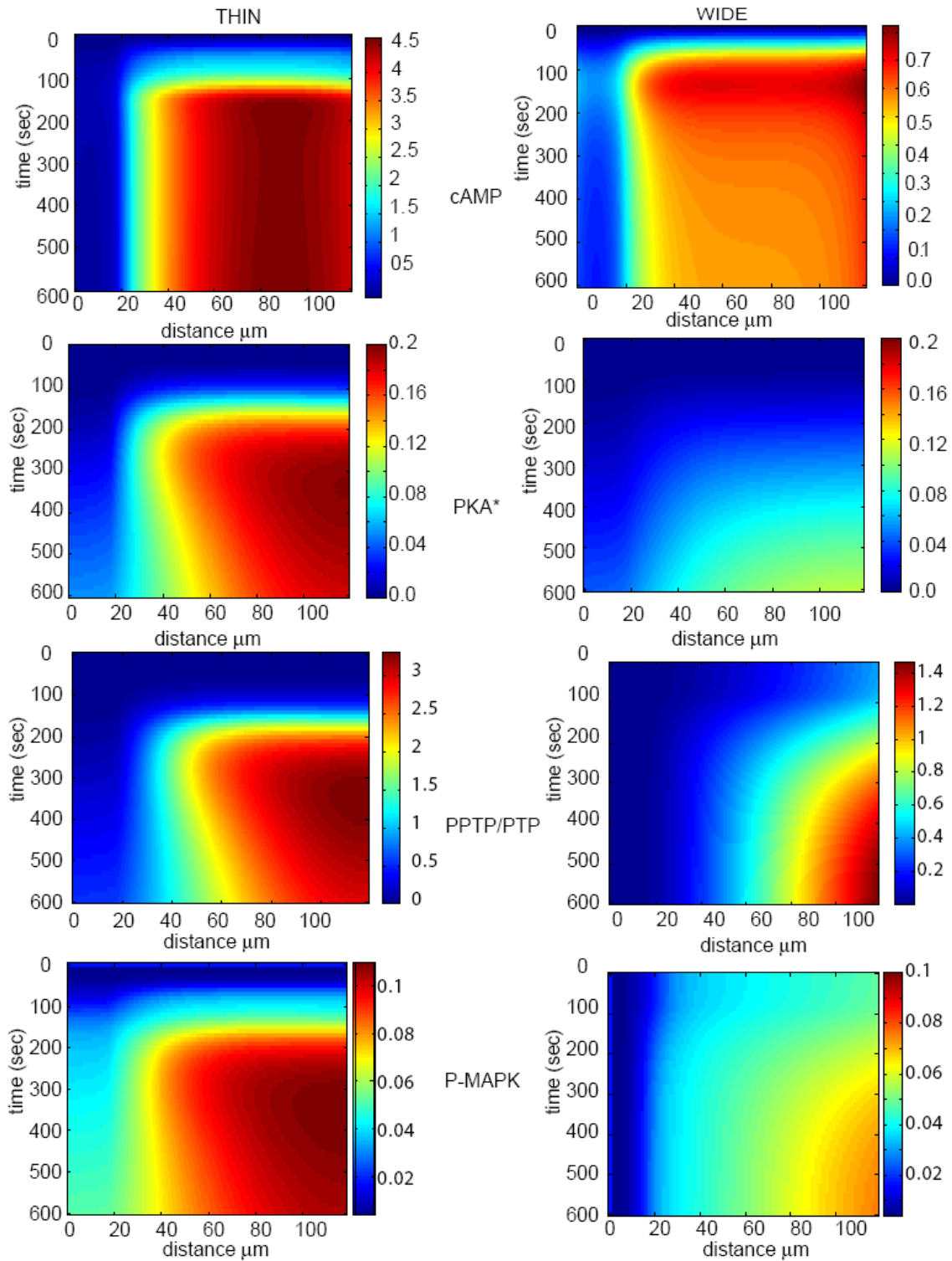


Fig S25 The ratio of P-PTP to PTP is important in the transmittal of spatial information from cAMP to P-MAPK. kymographs comparing the dynamics of activated PKA, P-PTP/PTP ratio and P-MAPK in 1 μm (left panels) and 3 μm (right panels) dendritic diameter geometry.

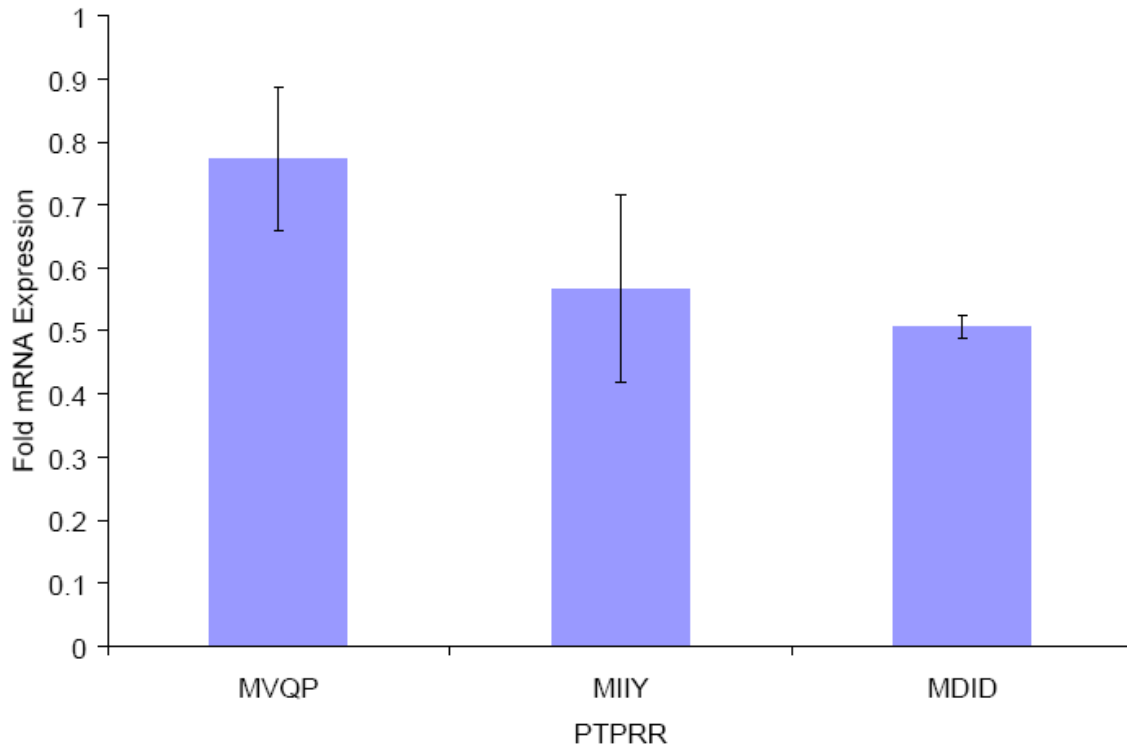


Fig S26 mRNA expression of PTPRR isoforms targeted by antisense oligonucleotide. The isoforms targeted by antisense oligonucleotides were MVQP (Pubmed ID= BC089186), MIIY (Pubmed ID=U14914), and MDID (Pubmed ID= D64050). Their expression was compared to mRNA from scrambled-treated tissue, and normalized with the expression of the housekeeping gene ribosomal protein rPL7.

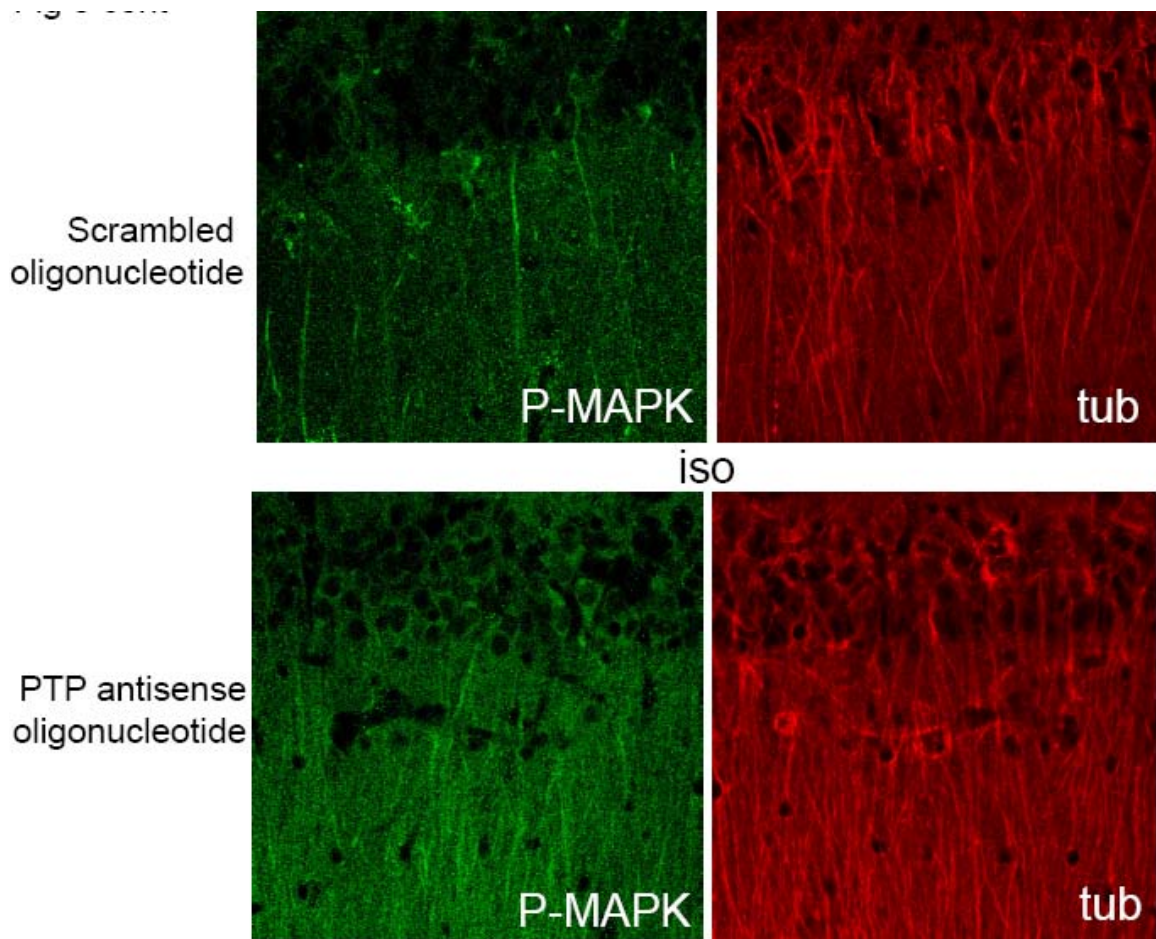


Figure S27 Reduction in PTP expression leads to isoproterenol-activation of MAPK in both cell body and dendrites. Confocal images of P-MAPK (green) and tubulin (red) immunofluorescence of CA1 hippocampal neurons in tissue slices. Hippocampal slices from rats injected with PTP antisense oligonucleotides (bottom) or its scrambled form (top) were treated with vehicle, or with 10 μ M isoproterenol for 20 min (Iso). Slices were subsectioned and stained with P-MAPK antibodies and visualized with confocal microscopy.

Table S1 - Initial Concentrations of Components used in the Spatial Models

| Component | Compartment | Concentration | Units | Diffusion ($\mu\text{m}^2/\text{s}$) | References and notes |
|------------------|--------------------|----------------------|----------------------------|--|-----------------------------|
| BAR | membrane | 94 | molecules/ μm^2 | | (S15) |
| G_protein | cytoplasmic | 3.6 | μM | 6.0 | (S15) |
| ATP | cytoplasmic | 5000 | μM | 300 | (S2) |
| AC | membrane | 300 | molecules/ μm^2 | - | (S15) |
| PKA (R2C2) | cytoplasmic | 0.2 | μM | 3.0 | (S16) |
| PDE4 | cytoplasmic | 0.4 | μM | 5.0 | (S2) |
| PP2A | cytoplasmic | 0.1 | μM | - | (S2) |
| MEK | cytoplasmic | 0.18 | μM | 7.0 | (S17) |
| B_Raf | cytoplasmic | 0.2 | μM | 6.0 | (S18) |
| AMP | cytoplasmic | 1000 | μM | 300.0 | (S2) |
| Iso | extracellular | 1 | μM | 300.0 | Saturating concentration |
| MAPK | cytoplasmic | 0.36 | μM | 7.0 | (S19) |
| PTP | cytoplasmic | 0.2 | μM | 6.0 | Estimated* |
| PDE_high_km | cytoplasmic | 0.5 | μM | 5.0 | Estimated* |
| GRK | cytoplasmic | 0.001 | μM | 6.0 | Estimated* |
| PPase_PDE | cytoplasmic | 0.2 | μM | - | Estimated* |
| PP1 | cytoplasmic | 0.1 | μM | - | Estimated* |

* Although, experimentally determined concentration values for these components were not available, we obtained estimated concentrations values by parameter scanning to obtain simulated input-output relationships that matched experimentally determined input-output relationships.

Table S2 Kinetic Reactions and Parameters

| | Reaction | | Parameters | References and Notes |
|------------------------------|---|------|---|----------------------|
| membrane reactions | | | | |
| 1 | iso + BAR \rightleftharpoons iso_BAR | Kf | 1.0000 $\mu\text{M}^{-1}\cdot\text{s}^{-1}$ | (S20) |
| | | Kb | 0.2000 s^{-1} | |
| 2 | G_protein + BAR \rightleftharpoons G_BAR | Kf | 0.3000 $\mu\text{M}^{-1}\cdot\text{s}^{-1}$ | (S21) |
| | | Kb | 0.1000 s^{-1} | |
| 3 | iso + G_BAR \rightleftharpoons iso_G_BAR | Kf | 1.0000 $\mu\text{M}^{-1}\cdot\text{s}^{-1}$ | (S20) |
| | | Kb | 0.0620 s^{-1} | (S22) |
| 4 | iso_BAR + G_protein \rightleftharpoons iso_G_BAR | Kf | 10.0000 $\mu\text{M}^{-1}\cdot\text{s}^{-1}$ | (S21) |
| | | Kb | 0.1000 s^{-1} | |
| 5 | iso_G_BAR \rightleftharpoons iso_BAR + G_GTP + bg | Kf | 0.0250 s^{-1} | (S23) |
| | | Kb | 0.0000 | |
| 6 | AC + ATP \rightarrow cAMP | Km | 1030.0000 μM | (S24) |
| | | Kcat | 0.2000 $\cdot\text{s}^{-1}$ | |
| 7 | AC + Gs_GTP \rightleftharpoons AC_Gs | Km | 500.0000 $\mu\text{M}^{-1}\cdot\text{s}^{-1}$ | (S25) |
| | | Kcat | 1.0000 s^{-1} | |
| 8 | ATP + AC_Gs \rightarrow cAMP | Km | 3.15 μM | (S24) |
| | | Kcat | 8.5000 $\cdot\text{s}^{-1}$ | |
| cytoplasmic reactions | | | | |
| 9 | G_GTP \rightleftharpoons G_GDP | Kf | 0.0670 $\mu\text{M}^{-1}\cdot\text{s}^{-1}$ | (S23) |
| | | Kb | 0.0000 s^{-1} | |
| 10 | G_GDP + bg \rightleftharpoons G_protein | Kf | 6.0000 $\mu\text{M}^{-1}\cdot\text{s}^{-1}$ | (S2) |
| | | Kb | 0.0000 s^{-1} | |
| 11 | cAMP + R2C2 \rightleftharpoons cAMP_R2C2 | Kf | 0.0059 $\mu\text{M}^{-1}\cdot\text{s}^{-1}$ | (S26, S27) |
| | | Kb | 0.0003 s^{-1} | |
| 12 | cAMP + cAMP_R2C2 \rightleftharpoons cAMP2_R2C2 | Kf | 0.0059 $\mu\text{M}^{-1}\cdot\text{s}^{-1}$ | (S26, S27) |
| | | Kb | 0.0003 s^{-1} | |
| 13 | cAMP + cAMP2_R2C2 \rightleftharpoons cAMP3_R2C2 | Kf | 8.3500 $\mu\text{M}^{-1}\cdot\text{s}^{-1}$ | (S26, S27) |
| | | Kb | 0.0167 s^{-1} | |
| 14 | cAMP + cAMP3_R2C2 \rightleftharpoons PKA | Kf | 8.3500 $\mu\text{M}^{-1}\cdot\text{s}^{-1}$ | (S26, S27) |
| | | Kb | 0.0167 s^{-1} | |
| 15 | cAMP + PDE4 \rightarrow AMP | Km | 1.3000 μM | (S28, S29, S30) |
| | | Kcat | 8.0000 $\cdot\text{s}^{-1}$ | |
| 16 | cAMP + highKm_PDE \rightarrow AMP | Km | 15.0000 μM | Estimated* |
| | | Kcat | 8.0000 $\cdot\text{s}^{-1}$ | |
| 17 | PDE4 + PKA \rightarrow PDE4_P | Km | 0.5000 μM | (S31) |
| | | Kcat | 10.0000 $\cdot\text{s}^{-1}$ | |
| 18 | cAMP + PDE4_P \rightarrow AMP | Km | 1.3000 μM | (S31, S32) |
| | | Kcat | 20.0000 $\cdot\text{s}^{-1}$ | |
| 19 | PDE4_P + ppase_PDE \rightarrow PDE4 | Km | 8.0000 μM | Estimated* |
| | | Kcat | 5.0000 $\cdot\text{s}^{-1}$ | |
| 20 | bRaf + PKA \rightarrow bRaf_active | Km | 0.5000 μM | Estimated* |
| | | Kcat | 10.000 $\cdot\text{s}^{-1}$ | |
| 21 | bRaf_active + PP2A \rightarrow bRaf | Km | 15.7000 μM | (S2) |
| | | Kcat | 5.0000 $\cdot\text{s}^{-1}$ | |
| 22 | MEK + bRAF_active \rightarrow MEK_active | Km | 0.1591 μM | (S33) |
| | | Kcat | 0.1050 $\cdot\text{s}^{-1}$ | |

| | | | | | |
|----|---|------|---------|------|------------|
| 23 | MEK_active + PP2A -> MEK | Km | 15.7000 | μM | (S2) |
| | | Kcat | 5.0000 | .s-1 | |
| 24 | MAPK + MEK_active -> MAPK_active | Km | 0.0465 | μM | (S17, S34) |
| | | Kcat | 0.1500 | .s-1 | |
| 25 | MAPK_active + PP2A -> MAPK | Km | 0.7700 | μM | (S35) |
| | | Kcat | 0.6360 | .s-1 | |
| 26 | MAPK_active + PTP -> MAPK | Km | 0.4600 | μM | (S35) |
| | | Kcat | 1.0200 | .s-1 | |
| 27 | PTP + PKA -> PTP_P | Km | 0.1000 | μM | (S36) |
| | | Kcat | 0.2000 | .s-1 | |
| 28 | MAPK_active + PTP_P -> MAPK | Km | 9.0000 | μM | (S36) |
| | | Kcat | 0.1000 | .s-1 | |
| 29 | PTP_P + PP1 -> PTP | Km | 6.0000 | μM | (S37) |
| | | Kcat | 5.0000 | .s-1 | |

Kinetic Reactions and their Parameters

Enzymatic Reaction ->

Mass Action Reaction <=>

Enzymes in **bold** type

* Parameters for these reactions were estimated by parameter scanning, to obtain simulated input-output relationships that matched experimentally determined input-output relationships.

Table S3. Geometries and Simulation Details











| Geometry | Figure | Size (μm) | Mesh (elements) | Timestep (s) | Sampling rate | References | |
|---|----------------------|--------------------------------------|--------------------|---------------------|---------------|------------|-------|
|  | neuro1 | 1,2, S4-5 | 150x136 50 x 30 | 318x288 230 x 76 | 1.00E-04 | 50000 | (S11) |
|  | Neuro-FRET1 | 1 | 60.4x179.2 | 116x348 | 0.001 | 30000 | - |
|  | Neuro-FRET2 | 3 | 202.5x80.8 | 239x96 | 0.001 | 15000 | - |
|  | Neuro2 | 4 | 175x167 | 175x167 | 0.001 | 20000 | - |
|  | Simple_1 Simple_3 | 1-5 S2-3, S8-14, S16-18 S20-22 | 122.5x22.5 | 273x43 | 0.001 | 10000 | - |
|  | fret1 | S5 | 120 x 103 | 216 x 188 | 1.00E-04 | 200000 | (S10) |
|  | 3D | S20 | 130x30x30 | 134x31x31 | 0.001 | 90000 | - |

Table S4 Fitted Constants used in Mathematical Analysis

| Geometry | Component | Condition | k_1 | k_2 | th_{col_sd} |
|---|------------------|------------------|---------|--------|----------------|
|  | cAMP | normal | 0.53459 | 1.8199 | 0.85 |
|  | cAMP | reduced PDE4 | 0.54718 | 1.1917 | 0.85 |
|  | PKA | normal | 0.57679 | 1.1869 | 0.7 |

The values for k_1 and k_2 used in equation1 change with the different geometries and components. The values in this table were obtained by curve fitting as described in fig S6.

Table S5- Supplemental Movies

| Movie | Geometry | Figure | Component shown | Conditions |
|--------------|-----------------|---------------|--|---|
| SM1 | Neuro2 | 1-2 | cAMP (top), P-MAPK (middle) and PKA (bottom) | isoproterenol stimulation of cAMP production, PKA and MAPK activation |
| SM2 | FRET1 | 1 | cAMP FRET | Isoproterenol stimulated |
| SM3 | FRET2 | 3 | cAMP FRET | Rolipram pretreatment Isoproterenol stimulated |
| SM4 | Simple_w | 3 | P-MAPK (top), PKA (middle) cAMP (bottom) | isoproterenol stimulation of cAMP production, PKA and MAPK activation |
| SM5 | Simple_w | 3 | P-MAPK (top), PKA (middle) cAMP (bottom) | isoproterenol stimulation of cAMP production, PKA and MAPK activation, with reduced concentration of PDE4 |
| SM6 | Simple_w | 5 | P-MAPK (top), PKA (middle) cAMP (bottom) | isoproterenol stimulation of cAMP production, PKA and MAPK activation with reduced concentration of PP1 and PP2A |

Table S6 Thiele Modulus (ϕ)

In order to determine the contribution of diffusion on the formation of the observed microdomains, we calculated the Thiele modulus (ϕ) for key components in the network. The Thiele modulus is a dimensionless number that is a measure of the diffusion and reaction component within a reaction-diffusion system (S38). When $\phi \ll 1$, diffusion presents a negligible resistance while a value of $\phi \gg 1$ represents a strong diffusion effect. The Thiele modulus ϕ , is calculated as follows:

$$\phi = \sqrt{\frac{k}{D}} L_{eff}$$

Where k is defined as

$$k = \frac{V_{max}}{K_m}$$

We define the effective length L_{eff} as the ratio of area to perimeter (S39).

We calculated ϕ for all the relevant components: cAMP, MAPK, b-Raf and MEK in both the dendrite and the cell body, for the downstream degradation/deactivation reactions. cAMP and MAPK produce microdomains, while b-Raf and MEK are uniformly distributed through out the cell. For this calculation we took the dimensions from the simplified geometry with a dendritic diameter of 3 μm , and a cell body diameter of 20 μm ($R=10 \mu\text{m}$, $L_{eff} = 5$) and the calculated, L_{eff} for the dendrite (assuming a rectangle, with a width of 3 μm , and a length of 100 μm) is 1.5. We found that the calculated value ϕ for all the components in the dendritic compartment was much less than 1 (see Table S6), suggesting that the diffusion contribution was small. From the calculated ϕ , it appears that all the reactions occurring in the dendrite have very little diffusion resistance.

We further explored the effect of varying the effective length L_{eff} and the P-MAPK diffusion coefficient on ϕ for the reaction involving PTP dephosphorylating P-MAPK (Fig S15A). Increasing L_{eff} resulted in a shift from a strong reaction component to a diffusion-driven regime. Increasing concentrations of PTP (Fig S15B) resulted in a decrease in the effective length at which the ϕ reaction-diffusion boundary occurs.

cell body

$L_{eff} = 5$

Degration/deactivation

| | cAMP | b_RAF | MEK | MAPK |
|--------------|-------------|--------------|------------|-------------|
| Km | 1.3 | 15.7 | 15.7 | 0.46 |
| Kcat | 8 | 5 | 5 | 1.02 |
| [E]nr | 0.4 | 0.1 | 0.1 | 0.2 |
| D | 300 | 6 | 7 | 7 |
| k | 2.462 | 0.032 | 0.032 | 0.443 |
| ϕ | 0.453 | 0.364 | 0.337 | 1.259 |

dendrite

$L_{eff} = 1.5$

Degration/deactivation

| | cAMP | b_RAF | MEK | MAPK |
|--------------|-------------|--------------|------------|-------------|
| Km | 1.3 | 15.7 | 15.7 | 0.46 |
| Kcat | 8 | 5 | 5 | 1.02 |
| [E]nr | 0.4 | 0.1 | 0.1 | 0.2 |
| D | 300 | 6 | 7 | 7 |
| k | 2.462 | 0.032 | 0.032 | 0.443 |
| ϕ | 0.136 | 0.109 | 0.101 | 0.378 |

Units: Michelis constant Km μM , turnover number Kcat 1/s, deactivating enzyme negative regulators concentration [E]nr is μM , Diffusion is $\mu\text{m}^2/\text{s}$. k and ϕ are dimensionless. For specifics please see (S38).

Table 7 Characteristic Path Length

We calculated the characteristic path length (CPL) in 2 dimensions as defined by Berg (S40) using the formula:

$$CPL = \sqrt{4D_A t}$$

Where D_A is the diffusion coefficient for each component, and t is time. CPL gives a measure of the maximal possible flux of a molecule given a certain diffusion coefficient and time. These values are shown in Table S7. At 600 sec, the CPL was greater than the maximal length (120 μm) of the geometry used in Fig 2 and S5-S14, suggesting that a mechanism other than diffusion may underlie the observed phenomena.

| | D | t = 600 s | t = 300 s | t = 150 s |
|-------|------------|------------------|------------------|------------------|
| cAMP | 700 | 1296.15 | 916.52 | 648.07 |
| | 300 | 848.53 | 600.00 | 424.26 |
| | 100 | 489.90 | 346.41 | 244.95 |
| B-Raf | 3 | 84.85 | 60.00 | 42.43 |
| | 6 | 120.00 | 84.85 | 60.00 |
| | 12 | 169.71 | 120.00 | 84.85 |
| MEK | 3 | 84.85 | 60.00 | 42.43 |
| | 7 | 129.61 | 91.65 | 64.81 |
| | 14 | 183.30 | 129.61 | 91.65 |
| MAPK | 3 | 84.85 | 60.00 | 42.43 |
| | 7 | 129.61 | 91.65 | 64.81 |
| | 14 | 183.30 | 129.61 | 91.65 |
| PDE | 1 | 48.99 | 34.64 | 24.49 |
| | 5 | 109.54 | 77.46 | 54.77 |
| | 10 | 154.92 | 109.54 | 77.46 |
| PTP | 3 | 84.85 | 60.00 | 42.43 |
| | 6 | 120.00 | 84.85 | 60.00 |
| | 12 | 169.71 | 120.00 | 84.85 |
| PKA | 3 | 84.85 | 60.00 | 42.43 |
| | 7 | 129.61 | 91.65 | 64.81 |
| | 14 | 183.30 | 129.61 | 91.65 |

Bold numbers indicate the diffusion coefficients (D, units $\mu\text{m}^2/\text{s}$) used in the numerical simulations.

References for Supplement

- S1. L. M. Loew, J. C. Schaff, *Trends Biotechnol* **19**, 401 (2001).
- S2. U. S. Bhalla, R. Iyengar, *Science* **283**, 381 (1999).
- S3. C. Chen, T. Nakamura, Y. Koutalos, *Biophys. J.* **76**, 2861 (1999).
- S4. D. Wisco *et al.*, *J Cell Biol* **162**, 1317 (2003).
- S5. D. C. Youvan *et al.*, *Biotechnology et alia* **3**, 1 (1997).
- S6. P. Tsokas *et al.*, *J. Neurosci.* **25**, 5833 (2005).
- S7. S. M. Taubenfeld, M. H. Milekic, B. Monti, C. M. Alberini, *Nat Neurosci* **4**, 813 (2001).
- S8. K. J. Livak, T. D. Schmittgen, *Methods* **25**, 402 (2001).
- S9. M. M. Bradford, *Anal Biochem* **72**, 248 (1976).
- S10. B. J. Bacskai *et al.*, *Science* **260**, 222 (1993).
- S11. G. a. G. Banker, K., *Culturing Nerve Cells*. . Ed., Cellular and Molecular Neuroscience (MIT Press, ed. 2, 1998).
- S12. Concentrations of components, kinetic reaction and geometries may be found in tables (S1-S3). Models may be found at <http://vcell.org>.
- S13. M. Mongillo *et al.*, *Circ Res* **95**, 67 (2004).
- S14. V. O. Nikolaev, M. Bunemann, L. Hein, A. Hannawacker, M. J. Lohse, *J Biol Chem* **279**, 37215 (2004).
- S15. S. R. Post, R. Hilal-Dandan, K. Urasawa, L. L. Brunton, P. A. Insel, *Biochem J* **311** (Pt 1), 75 (1995).
- S16. S. S. Taylor, J. A. Buechler, W. Yonemoto, *Annu Rev Biochem* **59**, 971 (1990).
- S17. R. Seger *et al.*, *J Biol Chem* **267**, 14373 (1992).
- S18. S. M. Storm, J. L. Cleveland, U. R. Rapp, *Oncogene* **5**, 345 (1990).
- S19. J. S. Sanghera, H. B. Paddon, S. A. Bader, S. L. Pelech, *J Biol Chem* **265**, 52 (1990).
- S20. S. A. Green, B. D. Holt, S. B. Liggett, *Mol Pharmacol* **41**, 889 (1992).
- S21. S. P. Fay, R. G. Posner, W. N. Swann, L. A. Sklar, *Biochemistry* **30**, 5066 (1991).
- S22. R. Seifert, U. Gether, K. Wenzel-Seifert, B. K. Kobilka, *Mol Pharmacol* **56**, 348 (1999).
- S23. D. R. Brandt, E. M. Ross, *J Biol Chem* **261**, 1656 (1986).
- S24. C. W. Dessauer, T. T. Scully, A. G. Gilman, *J Biol Chem* **272**, 22272 (1997).
- S25. P. G. Feinstein *et al.*, *Proc Natl Acad Sci U S A* **88**, 10173 (1991).
- S26. P. Hasler, J. J. Moore, G. M. Kammer, *Faseb J* **6**, 2735 (1992).
- S27. M. Zorn *et al.*, *FEBS Lett* **362**, 291 (1995).
- S28. G. B. Bolger *et al.*, *Biochem J* **328** (Pt 2), 539 (1997).
- S29. J. Lim, G. Pahlke, M. Conti, *J Biol Chem* **274**, 19677 (1999).
- S30. M. L. Reeves, B. K. Leigh, P. J. England, *Biochem J* **241**, 535 (1987).
- S31. C. Sette, M. Conti, *J Biol Chem* **271**, 16526 (1996).
- S32. S. J. MacKenzie, G. S. Baillie, I. McPhee, G. B. Bolger, M. D. Houslay, *J Biol Chem* **275**, 16609 (2000).
- S33. T. Force *et al.*, *Proc Natl Acad Sci U S A* **91**, 1270 (1994).
- S34. T. A. Haystead, P. Dent, J. Wu, C. M. Haystead, T. W. Sturgill, *FEBS Lett* **306**, 17 (1992).
- S35. B. Zhou, Z. X. Wang, Y. Zhao, D. L. Brautigan, Z. Y. Zhang, *J Biol Chem* **277**, 31818 (2002).
- S36. S. Paul *et al.*, *J Neurosci* **20**, 5630 (2000).
- S37. K. Nika *et al.*, *Biochem J* **378**, 335 (2004).

- S38. R. Bird, Stewart WE, Lightfoot EN, *Transport Phenomena* (Wiley Press, 1960).
- S39. I. C. Schneider, E. M. Parrish, J. M. Haugh, *Biophys J* **89**, 1420 (2005).
- S40. H. C. Berg, *Random Walks in Biology* (Princeton University Press, 1993).